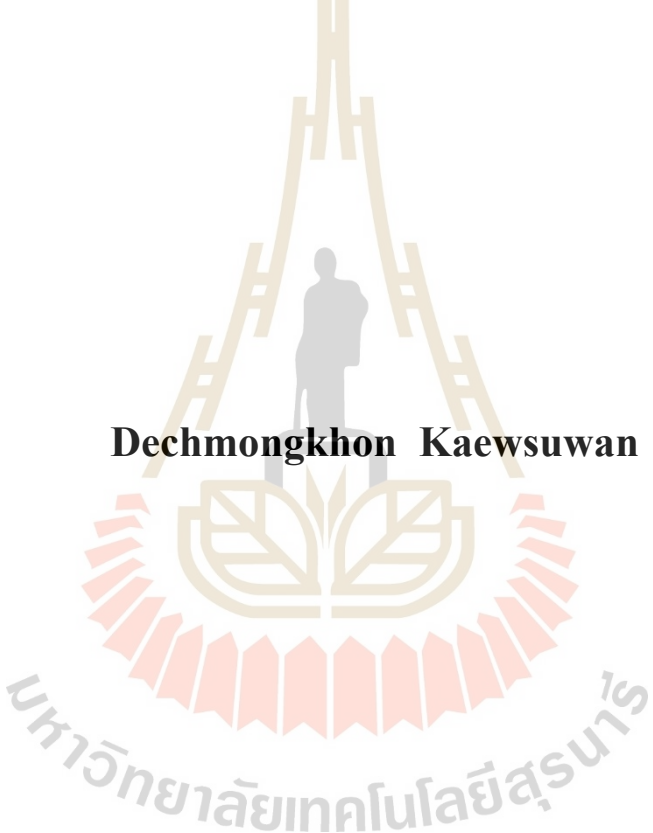


**PREPARATION OF TIN DIOXIDE QUANTUM DOT ON
SILICON SUBSTRATE BY MOLECULAR
BEAM DEPOSITION**



Dechmongkhon Kaewsuwan

**A Thesis Submitted in Partial Fulfillment of the Requirements for the
Degree of Master of Science in Applied Physics
Suranaree University of Technology
Academic Year 2019**

การเตรียมควอนตัมคอตทิงไดออกไซด์บนซิลิกอนด้วยเทคนิค
โมเลกุลาร์บีมดีโพสิชัน

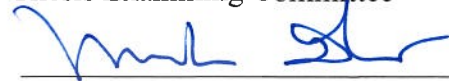


วิทยานิพนธ์นี้เป็นส่วนหนึ่งของการศึกษาตามหลักสูตรปริญญาวิทยาศาสตรมหาบัณฑิต
สาขาวิชาฟิสิกส์ประยุกต์
มหาวิทยาลัยเทคโนโลยีสุรนารี
ปีการศึกษา 2562

**PREPARATION OF TIN DIOXIDE QUANTUM DOT ON
SILICON SUBSTRATE BY MOLECULAR BEAM DEPOSITION**

Suranaree University of Technology has approved this thesis submitted in partial fulfillment of the requirement for a Master's Degree.

Thesis Examining Committee



(Assoc. Prof. Dr. Panomsak Meemon)

Chairperson



(Assoc. Prof. Dr. Saroj Rujirawat)

Member (Thesis Advisor)



(Prof. Dr. Rattikorn Yimnirun)

Member



(Assoc. Prof. Dr. Prayoon Songsiriritthigul)

Member



(Dr. Narong Chanlek)

Member



(Dr. Chanan Euaruksakul)

Member



(Assoc. Prof. Dr. Chatchai Jothityangkoon)

Vice Rector for Academic Affairs

and Quality Assurance



(Prof. Dr. Santi Maensiri)

Dean of Institute of Science

เดชมงคล แก้วสุวรรณ : การเตรียมควอนตัมดอททินไดออกไซด์บนซิลิกอนด้วยเทคนิค
โมเลกุลาร์บีมดีโพสิ (PREPARATION OF TIN DIOXIDE QUANTUM DOT ON
SILICON SUBSTRATE BY MOLECULAR BEAM DEPOSITION) อาจารย์ที่ปรึกษา :
รองศาสตราจารย์ ดร.สาโรช รุจิรวรรณ, 92 หน้า.

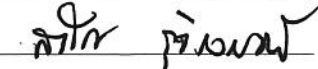
วิทยานิพนธ์ฉบับนี้รายงานการศึกษาการเตรียมควอนตัมดอททินไดออกไซด์บนแผ่น
ซิลิกอนระนาบ(001) ด้วยเทคนิคโมเลกุลาร์บีมดีโพสิชัน ร่วมกับการนำมาสัมผัสอากาศที่
อุณหภูมิห้อง โดยศึกษาพฤติกรรมของอะตอมทินบนแผ่นซิลิกอนด้วยเทคนิคการเปลี่ยนแปลง
รูปแบบการเลี้ยวเบนของรังสีเอกซ์พลังงานต่ำ (Low energy electron diffraction, LEED) และ กล้อง
จุลทรรศน์อิเล็กตรอนพลังงานต่ำ (Low energy electron microscopy) ในส่วนขององค์ประกอบ
ทางเคมีของทินไดออกไซด์บนแผ่นซิลิกอนระนาบ(001) ได้รับความศึกษาด้วยเทคนิคสเปกโตรสโกปี
ด้วยรังสีเอกซ์ (X-ray photoelectron spectroscopy, XPS) โครงสร้างอัฐฐานของทินไดออกไซด์
ได้รับความศึกษาด้วยกล้องจุลทรรศน์แรงอะตอม (Atomic force microscopy, AFM) ผลการศึกษา
พบว่าลักษณะพื้นผิวของทินไดออกไซด์เป็นไปตามโหมดการเกิดของ Volmer-Werber ซึ่งเป็น
โครงสร้าง 3 มิติ โดยมีขนาดประมาณ 100 นาโนเมตรซึ่งมีลักษณะเป็นจุดควอนตัม (Quantum dot)

การศึกษาผลของอุณหภูมิแผ่นซิลิกอนในขณะที่ปลูกพบว่าอุณหภูมิส่งผลต่อความหนาแน่น
และขนาดของควอนตัมดอท โดยพบว่าแผ่นซิลิกอนที่อุณหภูมิ 225 องศาเซลเซียส พบจุดควอนตัม
มีขนาดเล็กที่สุดประมาณ 80 นาโนเมตร โดยปกคลุมพื้นที่ของแผ่นซิลิกอนมากที่สุดประมาณ 53%
คุณสมบัติเชิงแสงของจุดควอนตัมของทินไดออกไซด์ได้รับความศึกษาด้วยเทคนิคการเรืองแสง
(photoluminescence spectroscopy, PL) พบว่ามีการเรืองแสงในช่วงแสงสีฟ้าช่วงประมาณ
(440-499 นาโนเมตร)

สาขาวิชาฟิสิกส์
ปีการศึกษา 2562

ลายมือชื่อนักศึกษา

ลายมือชื่ออาจารย์ที่ปรึกษา X

DECHMONGKHON KAEWSUWAN : PREPARATION OF TIN DIOXIDE
QUANTUM DOT ON SILICON SUBSTRATE BY MOLECULAR BEAM
DEPOSITION . THESIS ADVISOR : ASSOC. PROF.DR. SAROJ
RUJIRAWAT, Ph.D. 92 PP.

TIN DIOXIDE, MBE, SEMICONDUCTOR

This thesis presents the study on the molecular beam deposition of tin dioxide on silicon (001) substrate. The growth of tin dioxides was done by growing of Sn layers by molecular beam deposition technique and subsequently exposing to air at room temperature. The growth mechanism and effect of substrate temperature were real-time studied by in-situ low energy electron diffraction (LEED) and low energy electron microscopy (LEEM). The chemical composition of the grown tin dioxide was confirmed by X-ray photoelectron spectroscopy (XPS). The surface morphology of the grown tin dioxide was investigated by atomic force microscopy (AFM). It was found that growth follows the Volmer-Werber island growth mode. The three-dimensional structures of tin dioxide with a size of approximately 100 nm were formed which appear to be quantum dots.

The substrate temperatures of between 150-300°C do not significantly affect the growth. It was found that the SnO₂ grown at different substrate temperatures have a similar morphology, but they are different in the density of the island on the Si substrate. The smallest quantum dot size of 80 nm was observed on the tin dioxide quantum dot grown at the substrate temperature of 225°C.

The optical property of the grown tin dioxide quantum dot was also studied by photoluminescence spectroscopy (PL). The photoluminescence emissions were observed in blue range approximately 440-490 nm.



School of Physics

Academic Year 2019

Student's Signature

A handwritten signature in black ink, appearing to be 'Am 18', written over a horizontal line.

Advisor's Signature

× A handwritten signature in black ink, appearing to be 'Sanj Rejirawat', written over a horizontal line.

ACKNOWLEDGEMENTS

First of all, I would like to express the deepest appreciation to my advisor Assoc. Prof. Dr. Saroj Rujirawat for his patience, motivation, inspiration, advice, experience supervision, and guidance since the early stage of this research as well as giving me outstanding throughout the work.

I would like to thank Prof. Dr. Rattikorn Yimnirun for his valuable advice throughout this work, Dr. Narong Chanlek for his advice on XPS analysis and opportunities to gain experiences at Beamline 5.3: SUT-NANOTEC-SLRI XPS, Dr. Chanan Euaruksakul for his guidance and advice on surface science analysis and Miss Thipusa Wongpinit for her advice on MBE experiment. I also would like to thank all the members of the group.

I would like to acknowledge the Synchrotron Light Research Institute (SLRI) (public organization), Thailand for the scholarship and this work has been partially supported by the Research Network NANOTEC program of the National Nanotechnology Center, NSTDA, Ministry of Higher Education, Science, Research and Innovation, Thailand. I also would like to thank The Center for Scientific and Technological Equipment at Suranaree University of Technology for the Atomic Force Microscope measurement.

Finally, I would like to express appreciation to my family for their great support and encouragement to me throughout my studies.

Dechmongkhon Kaewsuwan

CONTENTS

	Page
ABSTRACT IN THAI.....	I
ABSTRACT IN ENGLISH.....	II
ACKNOWLEDGEMENT.....	III
CONTENTS.....	V
LIST OF TABLES.....	IX
LIST OF FIGURES.....	VIII
LIST OF ABBREVIATIONS.....	XIV
CHAPTER	
I INTRODUCTION.....	1
II LITERATURE REVIEWS.....	3
2.1 Tin dioxide.....	3
2.2.1 Structure of tin oxide.....	3
2.2.2 Semiconductor property.....	6
2.2.1 Optical property.....	6
2.2 Nanostructures and applications of tin dioxide.....	7
2.3 Molecular Beam Epitaxy (MBE).....	13
2.3.1 Lattice mismatch.....	14
2.3.2 Growth modes and mechanism.....	15
2.3.3. Effect of substrate temperature.....	18

CONTENTS (Continued)

	Page
III MATERIALS AND METHODS.....	19
3.1 Experimental procedure.....	19
3.2 Experimental setup	19
3.3 Preparation of material source and substrate.....	23
3.4 Characterization techniques.....	24
3.4.1 Low energy electron microscope (LEEM).....	24
3.4.2 Low energy electron diffraction (LEED).....	25
3.4.3 Atomic force microscope (AFM).....	28
3.4.4 X-ray photoelectron spectroscopy (XPS).....	31
3.4.5 Photoluminescence spectroscopy (PL).....	33
IV RESULTS AND DISCUSSION.....	36
4.1 Study on the growth mechanism.....	36
4.2 Study on the effect of substrate temperature on the growth	44
V CONCLUSION.....	55
REFERENCES.....	57
APPENDICES.....	64
APPENDIX A SIZE AND AREA OF ISLAND MEASUREMENT.....	65
APPENDIX B COMPONENTS AND OPERATION OF E-FLUX ELECTRON BEAM EVAPORATOR.....	72
CURRICULUM VITAE.....	75

LIST OF TABLES

Table	Page
2.1 Physical properties of SnO and SnO ₂	3
2.2 Preparation methods of SnO ₂ used as ETLs in PSCs. The precursor, device configuration and PCE are also included.....	10
2.3 Morphologies and properties of the representative SnO ₂ based gas sensors.....	12
4.1 Relative atomic concentration of element of the grown sample calculated from XPS spectra.....	41
4.2 Relative atomic concentration of Sn compared with Si of the grown sample calculated from XPS spectra.	47
4.3 Percentage of metallic tin and tin dioxide of the grown samples calculated from XPS spectra.....	47

LIST OF FIGURES

Figure	Page
2.1 The unit cells of α -SnO and the distance (lower) of the tin matrix of SnO (W.K. Choi et al., 1997).	4
2.2 The symmetry space group P4/nm. The blue and red spheres represent the O and Sn atoms, respectively. (M. Alex Ganose et al., 2016).	4
2.3 The symmetry space group P4/nm of SnO ₂ . The blue and red spheres represent the O and Sn atoms, respectively. (D. Degler et al., 2017).	5
2.4 Crystal structure of SnO ₂ and atomic configurations of the (101) surfaces (W.K. Choi et al., 1997)	5
2.5 Photoluminescence of SnO (W. Guo et al., 2010).	7
2.6 Schematic illustration of the density of states of (a) a bulk, (b) 2D, (c) 1D, d) 0D of semiconductor nanostructure (D. Bera et al., 2010)	8
2.7 (a) Electroluminescence spectra (0.5V) of SnO ₂ sample and (b) electroluminescence vs intensity applied voltage.	9
2.8 (a) Transmission spectrum of SnO ₂ film coated on the FTO substrate and (b) the transmission spectrum of SnO ₂ film coated on the glass substrate. (G. Yang, 2018).	10
2.9 Response curves of the sensors based on tin oxide QD/MWCNT nanocomposites and pristine SnO ₂ QD upon H ₂ S upon H ₂ S exposure/ release cycles at 79 °C (H. Liueal, 2015).	12

LIST OF FIGURES (Continued)

Figure	Page
2.10 Schematic diagram of MBE growth.	13
2.11 Different stages of 2D layer-by-layer growth mechanism and corresponding intensity of the zero-order reflected RHEED beam as a function of growth time.....	15
2.12 Schematic representation of the three growth modes, as a function of the coverage θ in ML: (a) Volmer–Weber growth; (b) Stranski–Krastanov growth; (c) layer-by-layer, or Frank–van der Merwe growth. (J. A. Venables, 2000)....	16
2.13 Equilibrium phases diagram showing growth modes of strained heteroepitaxial deposits on mismatched substrates as functions of coverage and lattice mismatch. (S. Franch, 2013)	17
2.14 AFM images of the deposited SnO ₂ films. The films were deposited respectively at substrate temperatures of (a) 648 K, (b) 701 K, (c) 773 K, (d) 873 K, and (e) 1023 K., (S. Hishita, 2010)	18
3.1 Flow charts of the experimental procedure.....	21
3.2 (a) Schematic diagram and (b) photograph of the MBE system at BL3.2Ub: PEEM, SLRI, Thailand.....	22
3.3 Photograph of the sample holder.....	23
3.4 LEED pattern of Si (001) substrate after flashed annealing at 1050°C.....	23

LIST OF FIGURES (Continued)

Figure	Page
3.5 Schematic of the LEEM experiment.....	24
3.6 Principle of LEED.	25
3.7 Schematic diagram of electron diffraction principle.	26
3.8 Real space and reciprocal space of face center cubic or fcc(110) structure.....	26
3.9 Atomic structure and diffraction pattern of fcc(100)	27
3.10 Schematic diagram of AFM measurement.....	29
3.11 Schematic diagram of C-AFM measurement.....	30
3.12 Schematic diagram of EFM measurement.....	30
3.13. Schematic diagram of XPS experiment.	31
3.14 Principle of photoluminescence.....	34
3.15 Schematic of photoluminescence experiment.....	35
4.1 LEED patterns of (a) the Si (100) substrate before the deposition (after flashed annealing at 1050°C) and after the deposition of (b) 60, (c) 120 and (d) 180 minutes.	37
4.2 LEEM images (Field of view of 50 μm) of (a) the Si (100) substrate before the deposition (after flashed annealing at 1050°C) and after deposition of (b) 60, (c) 120 and (d) 180 minutes.	38
4.3 Survey XPS spectrum of the grown layer.....	40
4.4 High resolution XPS spectra with the deconvolution of (a) Sn 3d and (b) O 1s (c) Si 2p peaks of the grown sample.	40

LIST OF FIGURES (Continued)

Figure	Page
4.5 Top view and 3-dimensional AFM images of the grown sample.	42
4.6 Topographic image of the sample and current profile in the cluster region (inset) obtained from the C-AFM measurement.....	43
4.7 Topographic image of the grown sample and the potential profile in the cluster region (inset) obtained from the EFM measurement.....	44
4.8 LEED patterns during the depositions at the different substrate temperatures...	45
4.9 Survey XPS spectra of the growth samples ST-150, ST-200, ST-225, ST-250, ST-275 and ST-300.....	46
4.10 High resolution XPS spectra of Sn 3d peaks of the grown samples ST-150, ST-200, ST-225, ST-250, ST-275 and ST-300.....	48
4.11 AFM top view images of the samples grown at the different substrate temperatures.....	49
4.12 The relation between the size and atomic concentration of metallic tin.....	50
4.13. Plot between the surface coverage of the cluster on the Si substrate and substrate temperatures.....	50
4.14 3-dimensional AFM images of the grown samples ST-150, ST-200, ST-225, ST-250, ST-275 and ST-300.....	51
4.15 PL emission spectra of the grown samples ST-150, ST-200, ST-225, ST-250, ST-275 and ST-300.....	52

LIST OF FIGURES (Continued)

Figure	Page
4.16 Deconvolution of the PL emission spectrum of the ST-225 sample.....	52
4.17 Schematic model for different relaxation process in SnO ₂	54
A.1 Main window of ImageJ software.....	65
A.2 Main window of ImageJ software after import an image file.....	65
A.3 Process of scale setting.....	66
A.4 New window for adjustment known distance and unit of length.....	66
A.5 Window shows measurement command.....	67
A.6 Window after click measure command.....	67
A.7 Image after the estimation.....	68
A.8 “Threshold” command in the program.....	69
A.9 Adjustment the selected area for calculation.....	69
A.10 “Analyze Particles” command.....	70
A.11 “Bare Outlines” function in the show parameter.....	70
A.12 Window shows the result of area.....	71
B.1 General assembly drawing of evaporator.....	72
B.2 Evaporator from tetra company (a) beside of the evaporator (b) Top-view (c) inside copper jacket.....	73
B.3 Power supply for controlling the flux current(a), flux controller(b).....	74

LIST OF ABBREVIATIONS

Å	Angstrom
°C	Degree Celsius
h	hole
eV	Electron volte
3D	Three Dimension
3d	Three orbital
Ek	Kinetic Energy
kV	Kilo Volt
nA	Nano Ampere
PL	Photoluminescence
hr	hour
Al K α	Aluminum k alpha
XPS	X-ray photoelectron Spectroscopy
AFM	Atomic Force Microscope
MBE	Molecular Beam Epitaxy
LEED	Low Energy Electron Diffraction
LEEM	Low Energy Electron Microscope
IMFP	Inelastic Mean Free Path
NSTDA	National Science and Technology Development Agency
SLRI	Synchrotron Light Research Institute
BL3.2 PEEM	Beamline 3.2 Photoemission Electron Microscope

CHAPTER I

INTRODUCTION

Tin dioxide (SnO_2) is an interesting oxide semiconducting material which is found in many applications, such as, gas sensors (S. Das et al., 2014), solar cells (G. Yang et al., 2018), transistors (L. Mai et al., 2019), catalysts (B. Kumar et al., 2017), batteries and supercapacitors (JS. Chen et al., 2013). It is of high interest because it has high electron mobility, high optical transmittance in visible light and near ultraviolet range and high reflection in the near-infrared region, high stability, and low cost (H. Bendjedidi et al., 2015) (W. Gou et al., 2010).

SnO_2 nanostructures, such as thin film, nanoparticles, nanotubes, nanorods, nanowires, and quantum dots, have become very attractive in a wide variety of technological applications in different fields because of their high surface-to-volume ratio and enhanced material characteristics due to quantum confinement effects. Different SnO_2 nanostructures have been intensively studied and various methods have been proposed for the synthesis of SnO_2 nanostructures, for example, spin coating (S.T. Bahade et al., 2017), sputtering (G. Bai et al., 2019), sol-gel (S. Javed et al., 2019), chemical vapor deposition (Y. Yu et al., 2018), thermal oxidation (M. Kwoka et al., 2017) and molecular beam epitaxy (MBE) (S. Chakraborty).

MBE is a thin film growth technique that allows precise control of compositional and doping profiles and thicknesses. This technique has been intensively used for the growth of advanced materials, structures and nanostructures, especially, a

wide array of III-V semiconductor material systems. It is also suitable for the fabrications of despite its potential on the preparation of metal oxide nanostructures, only a few studies have been reported on the growth of SnO₂ by MBE method (D. Bera et al., 2010) (A. Samavati et al., 2015). In 2008, M.E. White et al used the Plasma-assisted MBE growth technique to fabricate the single-crystal SnO₂ films on the r-sapphire substrate (ME White et al., 2008). In 2010, Shunichi Hishita, et al. reported SnO₂ film was prepared by MBE and ionization of oxygen molecules on the TiO₂(110) substrate and studied the effect of the substrate temperature to the morphologies. (S. Hishita, 2010)

This thesis reports the growth and effect of substrate temperature on the growth of SnO₂ on Si (001) substrate (lattice mismatch 9%) by molecular beam deposition and subsequent oxidation in air at room temperature. The growth mechanism was studied by the low energy electron microscope (LEEM) and low energy electron diffraction (LEED). The grown SnO₂ will be characterized by atomic force microscopy (AFM) and X-ray photoelectron spectroscopy (XPS) The optical property is studied by the photoluminescence spectroscopy (PL).

This thesis is composed of five chapters. The introduction and signification of the study are given in this Chapter. The basic properties, reviews of the application of SnO₂, and basic principles of MBE growth are provided in Chapter II. The details of the experiment including the characterization techniques used in this work are described in Chapter III. The experimental result with discussion is reported in Chapter IV. Finally, the conclusion is given in Chapter V.

CHAPTER II

LITERATURE REVIEWS

This chapter gives a brief review of the properties of tin dioxide, its applications and the basic principle and physics of molecular beam epitaxy (MBE) technique.

2.1 Tin oxide

2.1.1 Structure of tin oxide

Tin oxide is an interesting semiconductor material because it can be either n-type and p-type depending on the structure and oxidation state Sn. Tin (II) monoxide is p-type semiconductor, while tin (IV) dioxide is n-type semiconductor. Physical properties of SnO and SnO₂ are shown in Table 2.1.

Table 2.1 Physical properties of SnO and SnO₂.

Physical properties	SnO	SnO ₂
Molar mass	134.71 g/mol	150.708 g/mol
Density	6.45 g/cm ³	6.95 g/cm ³
Melting point	1500-1630°C	1630°C
Boiling point	1800-1900°C	1800-1900°C
Magnetic susceptibility	- 19x10 ⁻⁶	-4.1x10 ⁻⁵ cm ³ /mol

Tin (II) monoxide (SnO) or stannous oxide structure consists of tin (II) covalently bonding to one oxygen atom. The oxygen atom in the center of the unit cell is surrounded by the 4 Sn atoms with the bond length of 2.23 Å (like a pyramid that

consists of one Sn and four O atoms). SnO has a layered structure (very similar to that of PbO) in the (001) direction with a Sn^{1/2}-O- Sn^{1/2} sequence. SnO has the symmetry space group P4/nmm (In figure 4.7) of tetragonal structure with lattice constants $a=b=3.802 \text{ \AA}$, $c=4.836 \text{ \AA}$, $c/a=1.27$ (S. Chakraborty et al., 2019). The Sn (2+) ions occupy the $(1/2, 0, 3/4)$ and $(0, 1/2, 1/4)$ sites of a unit cell as shown in Figure 2.1 and Figure 2.2. (W.K. Choi et al., 1997). The Van-der-Waals distance between two neighboring Sn layers is about 2.52 \AA .

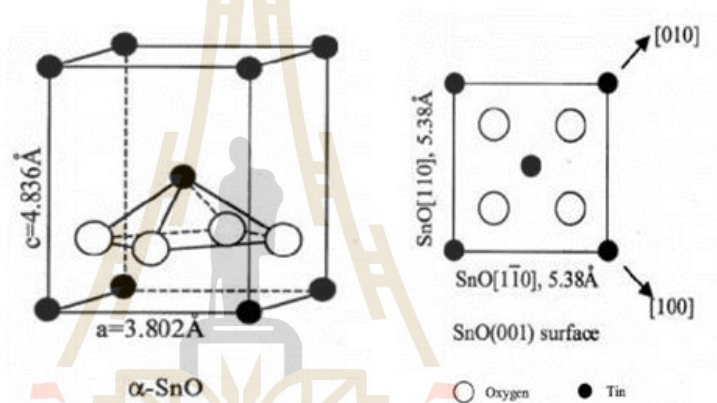


Figure 2.1 The unit cell of α -SnO and the distance (lower) of the tin matrix of SnO (W.K. Choi et al., 1997).

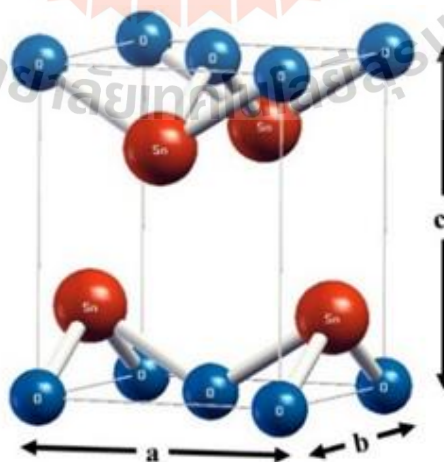


Figure 2.2 The symmetry space group P4/nm of SnO. The blue and red spheres represent the O and Sn atoms, respectively. (M. Alex Ganose et al., 2016).

Tin dioxide (SnO_2) or stannic has a rutile structure. Sn atom is six-fold coordinated while the oxygen atoms are threefold coordinated. Sn atoms are surrounded by distorted octahedrons of O atoms, or each oxygen atom is coordinated by three tin atoms as shown in Figure 2.3.

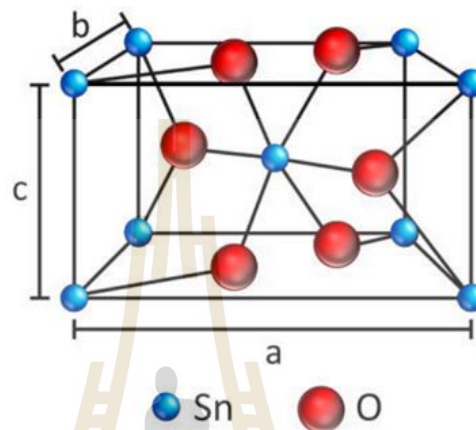


Figure 2.3 The symmetry space group $P4/nm$ of SnO_2 . The blue and red spheres represent the O and Sn atoms, respectively. (D. Degler et al., 2017).

Rutile SnO_2 has tetragonal space group $P4/nm$ symmetry, belonging to the tetragonal system. The lattice parameters are $\alpha = \beta = \gamma = 90^\circ$, $a = b = 0.474 \text{ nm}$, $c = 0.319 \text{ nm}$ (W.K. Choi et al., 1997) as shown in Figure 2.4.

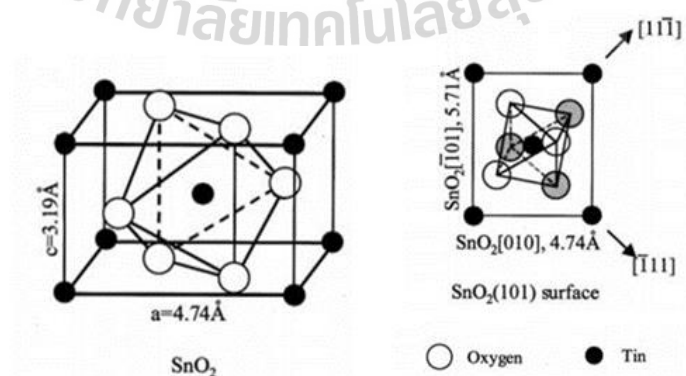


Figure 2.4 Crystal structure of SnO_2 and atomic configurations of the (101) surfaces (W.K. Choi et al., 1997).

2.1.2 Semiconductor property

Tin monoxide generally exhibits a p-type semiconductor nature with the direct bandgap of between 2.7-3.4 eV (W.Guo et al., 2010). Conversion into the n-type semiconductor can be achieved upon doping with Y or Sb, making SnO a bipolar conducting oxide. SnO has attracted much attention because of its high hole mobility, the presence of intrinsic Sn vacancies or oxygen interstitials. (J. Um et al., 2014) (H. Yeon Kim et al., 2019)

Tin dioxide is an n-type semiconductor material which has a bandgap of between 3.6-4.3 eV without doping (P. Jain et al., 2017). SnO₂ has been widely used as a transparent conducting oxides (TCO) material. It can be converted to p-type semiconductor by doping acceptors in SnO₂.

2.1.3 Optical property

Tin oxide and tin dioxide are the most widely used materials for photovoltaic cell because they have a highly optical transparency. They are also used in optoelectronic and display devices such as light emitting diode (LED). SnO has a light yellowish color with average optical transparency of between 70%-85% as shown in the optical transmittance spectrum in Figure 2.5. (W. Guo et al., 2010). SnO₂ has an optical transmittance of about 97% in visible and near ultraviolet range due to its wide bandgap and small reflective index of <2% (A. F. Khan et al., 2010).

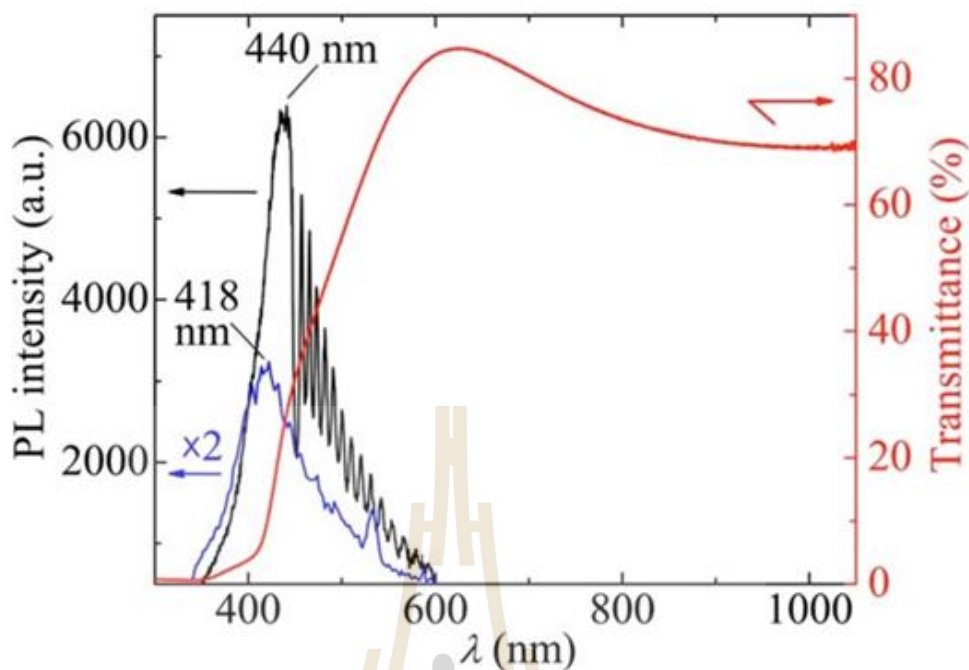


Figure 2.5 Photoluminescence and optical transmittance spectra of SnO (W. Guo et al., 2010).

2.2 Nanostructures and applications of tin dioxide

Nanostructured materials are materials, which have the characteristic length scale on the order of a few nanometers. (H. Gleiter, 2000). The nanostructured materials are of great interest as they can bridge the gap between the bulk and molecular levels. The distinct variations of optical, magnetic, and electronic properties occur with a variation of particle size <100 nm. This leads to entirely new avenues for applications, especially in electronics, optoelectronics, and biology. Generally, nanostructured materials can be classified based on the shape as zero-dimension e.g., carbon 60, one-dimension e.g., carbon nanotube and nanowires, two-dimension e.g., thin film and surface and three-dimension, e.g., graphite bulk. In the case of semiconductor, the number of dimensions of semiconductor nanostructure affects the electronic structure, such as the quantum

state and energy bandgap. The illustration of the density of states of a bulk, 2-dimensional (D), 1-dimensional and 0-dimensional of semiconductor nanostructures is shown Figure 2.6. The nanostructures are often called as (D. Bera et al., 2010)

- (1) bulk semiconductor for three- dimension
- (2) quantum wells for two-dimension
- (3) quantum wires for one-dimension
- (4) quantum dots for zero-dimension

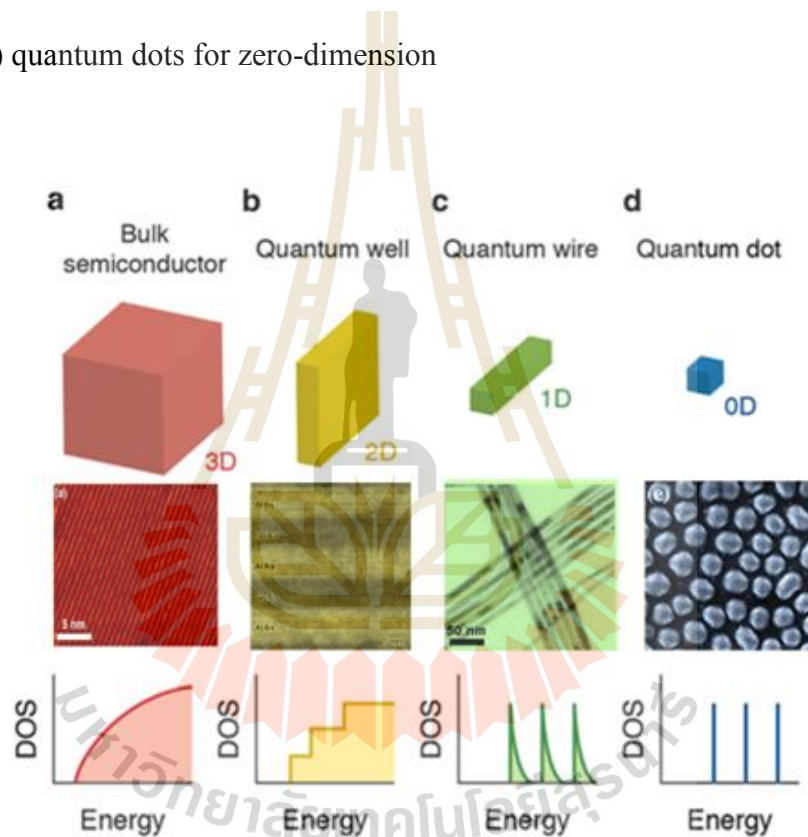


Figure 2.6 Schematic illustration of the density of states of (a) a bulk, (b) 2D, (c) 1D, d) 0D of semiconductor nanostructure (D. Bera et al., 2010).

A number of development of nanostructures with different morphologies and applications of SnO₂ have been reported. In 2017, S.S. Nath et al. reported the study of SnO₂ quantum dot (QD) as nanolight emitting device at a very low bias with fast response speed on the order of 10⁻⁹ sec.

Figure 2.7(a) shows the electroluminescence (EL) of SnO₂ quantum dots as nano light emitting device. SnO₂ quantum dot exhibited an electroluminescence at around 580 nm at room temperature and it was believed that the emission is a result of the oxygen vacancy.

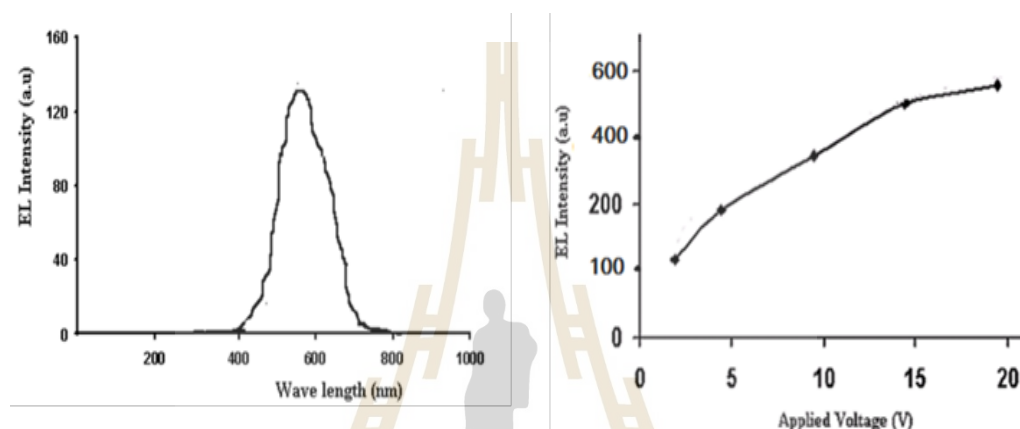


Figure 2.7 (a) Electroluminescence spectra (0.5V) of SnO₂ QDs and (b) electroluminescence vs intensity applied voltage (S.S. Nath et al., 2017).

Perovskite solar cell (PSCs) has rapidly become a hot area of research in photovoltaic. The impressively high efficiency was designed as the layer of the PSCs device. The layer of the PSCs usually consists of a transparent electrode, an n-type layer including a compact layer and mesoporous (mp) layer (optional), an intrinsic layer (hole transport layer) and the back-contact electrode. SnO₂ nanostructures such as quantum dots can be used as compact layers, mp layer and blocking layer in PSCs due to high electron mobility, wide bandgap and band alignment to perovskite.

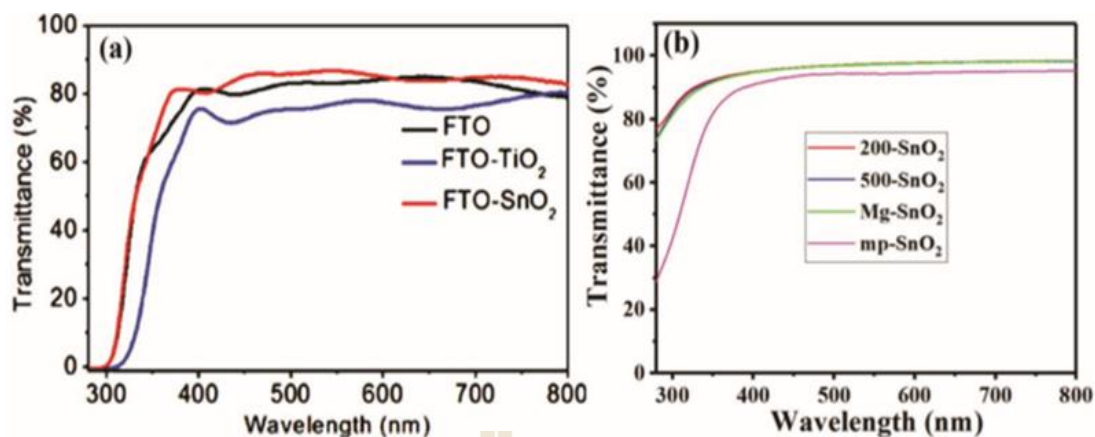


Figure 2.8 (a) Transmission spectrum of SnO₂ film coated on the FTO substrate and (b) the transmission spectrum of SnO₂ film coated on the glass substrate. (G. Yang, 2018)

In 2018, G. Yang et al., used the SnO₂ quantum dot films as ETLs whose transmittances even surpass 95% in the visible region shown in Figure 2.8(b). The efficient light management in the UV-visible region offers a photon passing through easily and being absorbed by the perovskite absorber. Other previous studies on SnO₂ nanostructures for PSCs are also given in Table 2.2.

Table 2.2 Preparation methods of SnO₂ used as ETLs in PSCs. The precursor, device configuration and PCE are also included.

Preparation Method	Precursor	Functional layer	PCE (%)	Ref.
Sol-gel	SnCl ₂	FTO/SnO ₂ /MAPbI ₃ /spiro/Au	17.2	W. J. Ke et al., 2015
CVD	SnCl ₂	ITO/SnO ₂ /MAPbI ₃ /spiro/Au	14.8	J. Barbe et al., 2017
Electrodeposition	SnCl ₂	ITO/SnO ₂ /MAPbI ₃ /spiro/Au	13.8	J. Y. Chen et al., 2017

Table 2.2 Preparation methods of SnO₂ used as ETLs in PSCs. The precursor, device configuration and PCE are also included. (Continued)

Preparation Method(cont.)	Precursor (cont.)	Functional layer (cont.)	PC(%) (cont.)	Ref. (cont.)
E-beam evaporation	SnO ₂ powder	FTO/SnO ₂ /MAFAPbBr/spiro/Au	18.2	J. Ma et al., 2017
Spray pyrolysis	Butyltin trichloride	AZO/BL-SnO ₂ /mp-SnO ₂ /MAPbI ₃ /Spiro/Au	13.1	B. Roose et al., 2016
Ball milling	C-SnO ₂ NPs	FTO/BL-SnO ₂ /mp-SnO ₂ /MAPbI ₃ /Spiro/Au	19.1	L. B. Xiong et al., 2018
Hydrothermal	Tin oxalate	FTO/hierarchical SnO ₂ /MAPbI ₃ /spiro/Au	16.17	Q. Liu et al., 2010
Spin coating	SnCl ₂	FTO/SnO ₂ QDs/ MAPbI ₃ / spiro/Au	16.97	G. Yang et al., 2018
Spin coating	SnCl ₂	FTO/SnO ₂ QDs/ MAPbI ₃ / spiro /Au	17.21	W. Ke et al., 2013

One of the most widely used applications for SnO₂ nanostructures are gas sensor for, such as, C₂H₅OH, CO, CO₂, H₂, NH₃, H₂S.

This is because SnO₂ exhibits n-type oxide conductivity and has high sensitivity, fast response and long-term stability. In 2015, Huan Liu et al., studied the hydrogen Sulfide (H₂S) gas sensor based on SnO₂ QD/multiwalled carbon nanotube (MWCNTs) nanocomposites. As shown in Figure 2.9, the SnO₂ QDs/MWCNT exhibited a high response upon exposure to H₂S, and response toward 50 ppm of H₂S at 70 °C was 108 with the response and recovery time being 23 and 44 seconds. This is because the SnO₂ quantum dot/MWCNT has extremely small size and high surface

active of semiconductor nanocrystals. Examples of the study on SnO₂ nanostructures as gas sensors are provided in Table 2.3

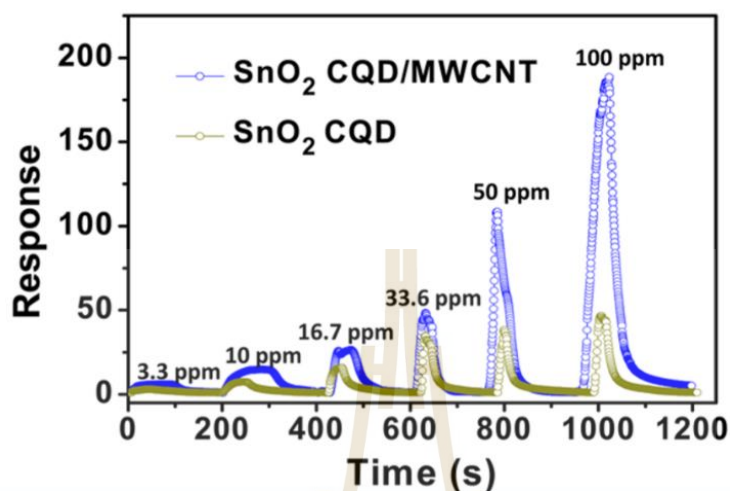


Figure 2.9 Response curves of the sensors based on SnO₂ QD/MWCNT nanocomposites and pristine SnO₂ QD upon H₂S upon H₂S exposure/release cycles at 79°C (H. Liu et al., 2015)

Table 2.3 Morphologies and properties of the representative SnO₂ based gas sensors.

Materials	Morphologies	Detection range (ppm)	Temperature(°C)	Target gas	Ref.
SnO ₂ -Co	Nanofiber	100-25,000	330	H ₂	L. Lui et al., 2010
SnO ₂ -Pt	Nanowire	10-100	300	H ₂	N. Van Hieu, et al., 2008
SnO ₂ -Pt	Thin film	1000-10,000	350	CH ₄	Min and Choi, 2005
SnO ₂	Thin film	10-100	300	C ₂ H ₄	Ahn et al., 2010
SnO ₂ /MWCNT	QDs+Nanotube	200-1200	70	H ₂ S	H. Liu et al., 2015
SnO ₂	QDs	133-1333	Room temp.	H ₂	J. Lui et al., 2019

2.3 Molecular Beam Epitaxy (MBE)

MBE is a widely used technique to grow high quality thin film of compound semiconductors, metals, or insulators. This technique allows precise control of compositional and doping profiles which is suitable for the preparation of advanced structures on a nanometer scale.

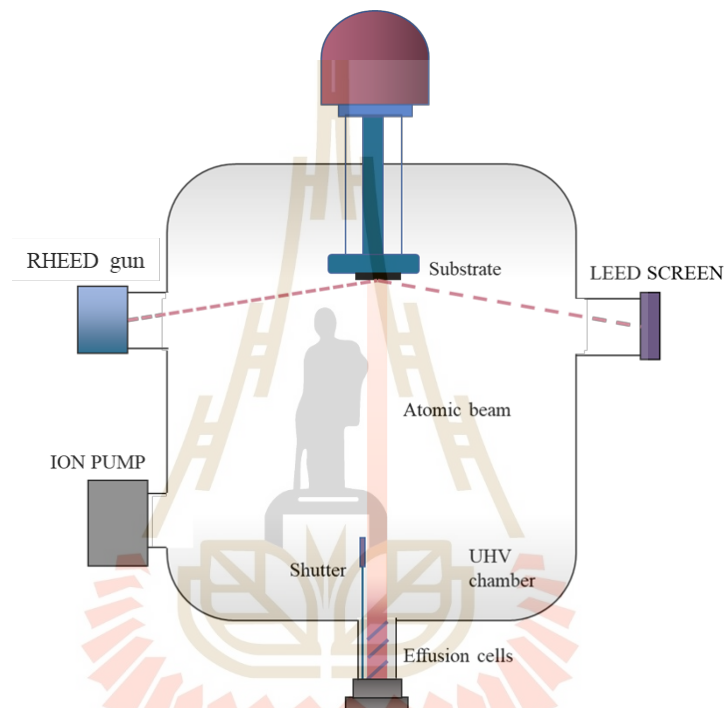


Figure 2.10 Schematic diagram of MBE growth.

The MBE is an epitaxial process that takes place in high vacuum or ultra-high vacuum (UHV), 10^{-8} – 10^{-12} Torr. A beam of neutral atoms or molecules is generated by evaporation or sublimation of suitable materials contained in ultra-pure crucible in a material source, called efficient cell as shown in Figure 2.10. The beams, which generally have thermal energy, are deposited on a flat substrate, which is held at a constant temperature depending on the specific type of materials. Deposited atoms adopt the orientation of the substrate and incorporate with the film. The layer or deposits

have the same crystalline structure with the substrate and the lattice parameter which differ from the substrate less than 10%. The most important aspect of MBE is the deposition rate (typically less than 3,000 nm per hour) that allows the films to grow epitaxially. These deposition rates require proportionally better vacuum to achieve the same impurity levels as other deposition techniques. The absence of carrier gases, as well as the ultra-high vacuum environment, result in the highest achievable purity of the grown films.

2.3.1 Lattice mismatch

The lattice mismatch is a parameter of the lattice between the in-plane lattice parameters of free- standing epilayer and substrate which can be defined as Equation (1).

$$\epsilon_0 = \frac{a_e - a_s}{a_s} \quad (2.1)$$

When; ϵ_0 is the lattice mismatched,

a_e is the in-plane lattice parameters of free- standing epilayer and

a_s is the lattice of the substrate.

Since 1980, the Monte Carlo's simulation have shown that the epitaxial growth takes place according to the layer by layer (2D) mechanism if the percentage of the lattice mismatch between epilayer and substrate is smaller than 2-3%. In 1987, Ghaisas a Madhukar studied the effect of both compressive and tensile strain occurring pronounced in RHEED oscillations as shown in Figure 2.11.

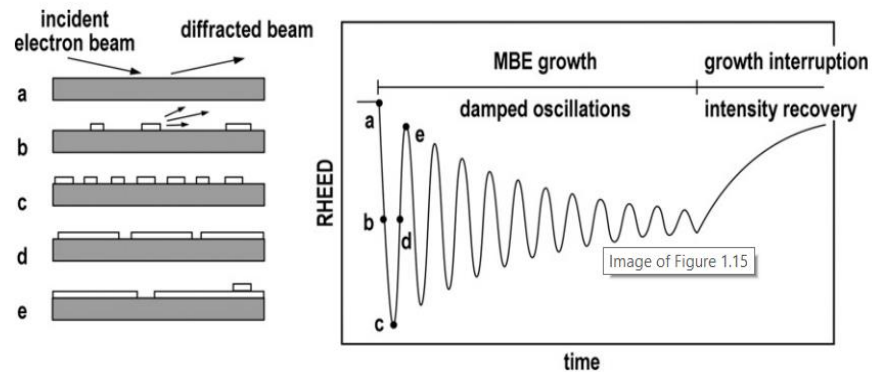


Figure 2.11 Different stages of 2D layer-by-layer growth mechanism and corresponding intensity of the zero-order reflected RHEED beam as a function of growth time.

For the high lattice mismatched, the growth of epitaxy is deposited under large compressive strain which will be shown as deposits -assemble in the island. The mechanism of island differs from the lowly lattice mismatch substrate. The island may have size smaller than the de Broglie wavelength of carrier. So, when islands are covered by appropriated confining layer they behave as quantum dot (S. Franchi, 2013).

2.3.2 Growth modes and mechanism

The MBE growth can be classified into three growth modes according to a much-quoted paper in *Zeitschrift für Kristallographie* (Bauer, 1958) as shown in Figure 2.12. These modes are Layer by layer or Frank–van der Merwe growth, Island or Volmer-Weber mode, and Stranski–Krastanov growth.

The layer-by-layer, or Frank–van der Merwe, growth mode arises because the atoms of the deposited material are more strongly attracted to the substrate than they are to themselves. On the contrary, the island, or Volmer–Weber mode is formed when

the deposit atoms are more strongly bound to each other than they are to the substrate.

For Stranski mode, the deposit atom can be grow a few layers and then become to island.

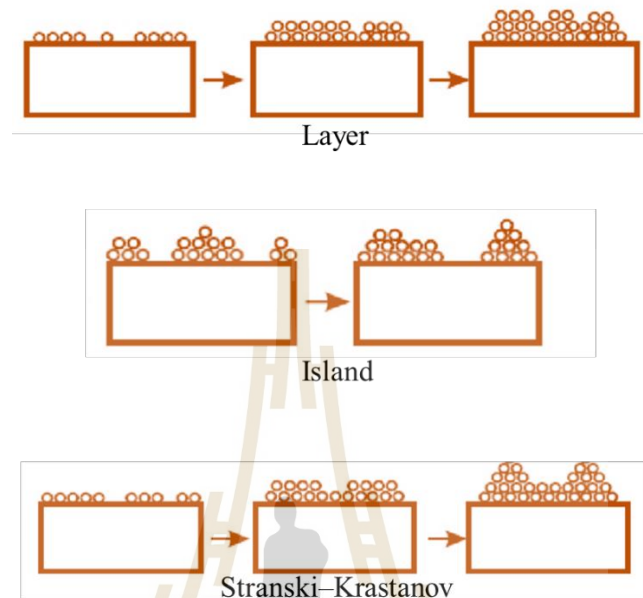


Figure 2.12 Schematic representation of the three growth modes, as a function of the coverage θ in ML: (a) Layer by layer or Frank–van der Merwe growth, (b) Island or Volmer-Weber mode, and (c) Stranski–Krastanov growth. (J. A. Venables, 2000) The layer-plus-island, or Stranski–Krastanov (SK) growth mode is an intermediate case, where layers form first, but then for one reason or another the system gets tired of this, and switches to islands. (J. A. Venables, 2000)

Daruka and Barabasi studied on the thermodynamic equilibrium models consisting of a substrate and a mismatched epitaxial deposit. The equilibrium property was investigated by a phase diagram, part of which is shown in Figure 2.13.

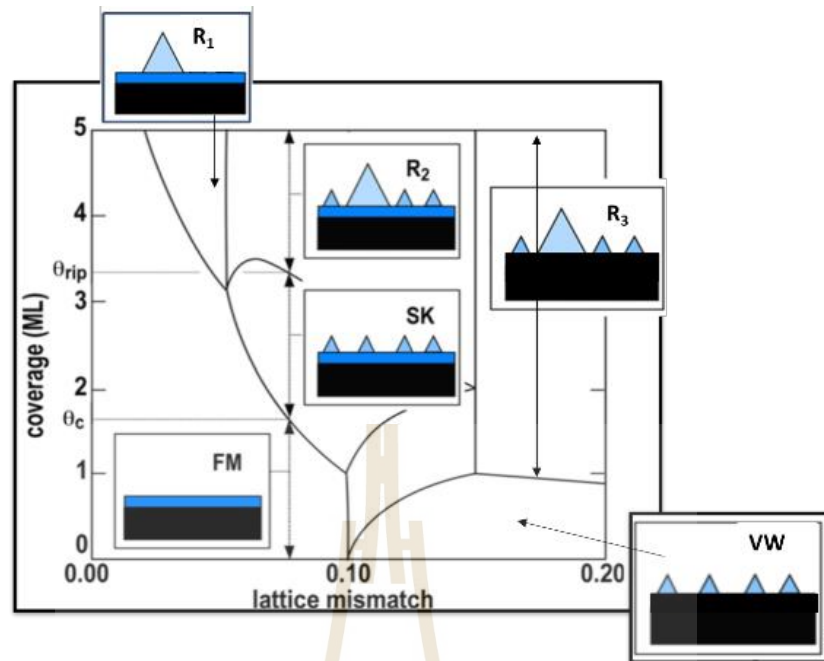


Figure 2.13 Equilibrium phases diagram showing growth modes of strained heteroepitaxial deposits on mismatched substrates as functions of coverage and lattice mismatch. (S. Franchi, 2013)

The diagram shows the different growth modes and stability of islands depending on coverage (θ), critical coverages (θ_c and θ_{rip}) and lattice mismatch (ϵ) between deposit and substrate. It can be divided into three case as:

- (i) $\theta < \theta_c$, the deposits occur the layer by layer or pseudomorphic,
- (ii) $\theta_c < \theta < \theta_{rip}$, partially relaxed stable island coexists on top of pseudomorphic, and
- (iii) $\theta > \theta_{rip}$, the stable island and large islands with uncontrolled size (ripened island). The critical coverage can be controlled to a certain extent by acting on (i) lattice mismatch, (ii) substrate temperature, and (iii) the growth process.

2.3.3 Effect of substrate temperature

In 2010, Shunichi Hishita, et al., reported the effect of the substrate temperature on the morphologies of the SnO₂ film on TiO₂ substrate, The film's surface morphology became smooth with increasing substrate temperature up to 773K and became rough at higher temperature as shown in Figure 2.14 (S. Hishita et al., 2010).

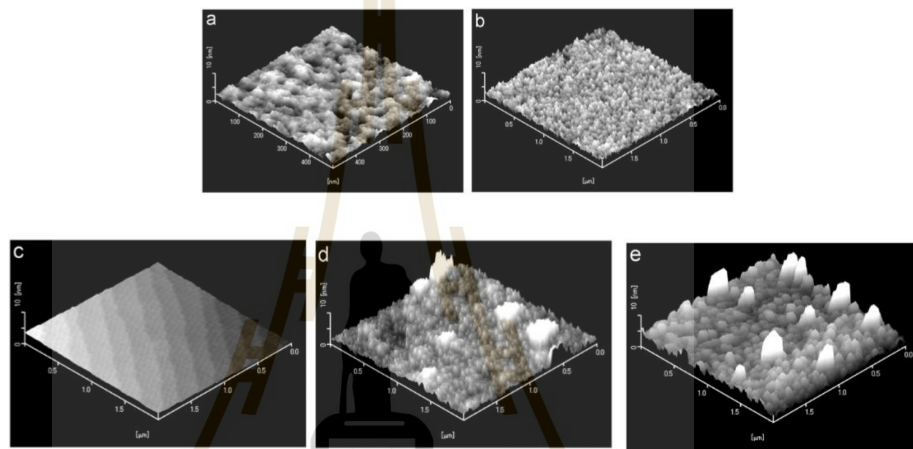


Figure 2.14 AFM images of the deposited SnO₂ films. The films were deposited respectively at substrate temperatures of (a) 648 K, (b) 701 K, (c) 773 K, (d) 873 K, and (e) 1023 K (S. Hishita, 2010).

CHAPTER III

MATERIALS AND METHOD

This chapter describes the details of experimental procedure, experimental setup, raw materials and characterization techniques used in this work.

3.1 Experimental procedure

In this thesis, the MBE growth of tin dioxide on silicon (100) substrate was studied. The growth of tin dioxide was carried out in two different steps. The first step is the deposition of tin layers by MBE technique and the second step is the exposure to air atmosphere at room temperature to oxidize the grown tin layers. The flow charts of experimental procedure are shown in Figure 3.1. The experiment was divided into two sections. The first section is to study the growth mechanism. In-situ LEEM and LEED were used to real-time monitor the growth process. AFM and XPS were used to characterize the grown layers. The second section is to study the effect of substrate temperature on the growth. The substrate temperature was varied between 150 - 300°C. In-situ LEED was used to monitor the growth and AFM, and XPS was used to characterize the grown layers. The optical property of the grown sample was also studied by PL

3.2 Experimental setup

The experiment was carried out at the molecular beam epitaxy (MBE) system installed at the end-station of Beamline (BL) 3.2b: Photoelectron Emission Microscope (PEEM), Synchrotron light research institute (Public Organization) (SLRI), Thailand. The schematic diagram and photograph of the system are shown in Figure 3.2. The system consists of three main vacuum chambers: the loaded lock chamber, preparation chamber, and experimental chamber. These chambers are separated by vacuum gate valve. The load-lock chamber is used for introduction/extraction of sample. The preparation chamber is used for preparation of sample. It has a base pressure of 5×10^{-4} Pa. In this chamber, a sample can be heated from room temperature to 500°C by heated filament. Different gases such as O_2 and N_2 can be also leaked into the chamber under the chamber pressure of less than 5×10^{-2} Pa. The experimental chamber is used for molecular beam epitaxial growth and characterizations of sample. It has a base pressure of less than 10^{-7} Pa. This chamber is installed with an electron beam evaporator used the tungsten filament (Tetra series of e-flux evaporator) which can be operated up to 1200°C . More details of the electron beam evaporator are given in appendix B. The sample holder can be heated up to 1200°C . The chamber is also installed with a spectroscopic photoemission and low-energy electron microscopy (SPELEEM) system (Elmitech's LEEM III). This allows to perform four in-situ characterization techniques including LEED, LEEM, XPS, and X-ray absorption spectroscopy (XAS).

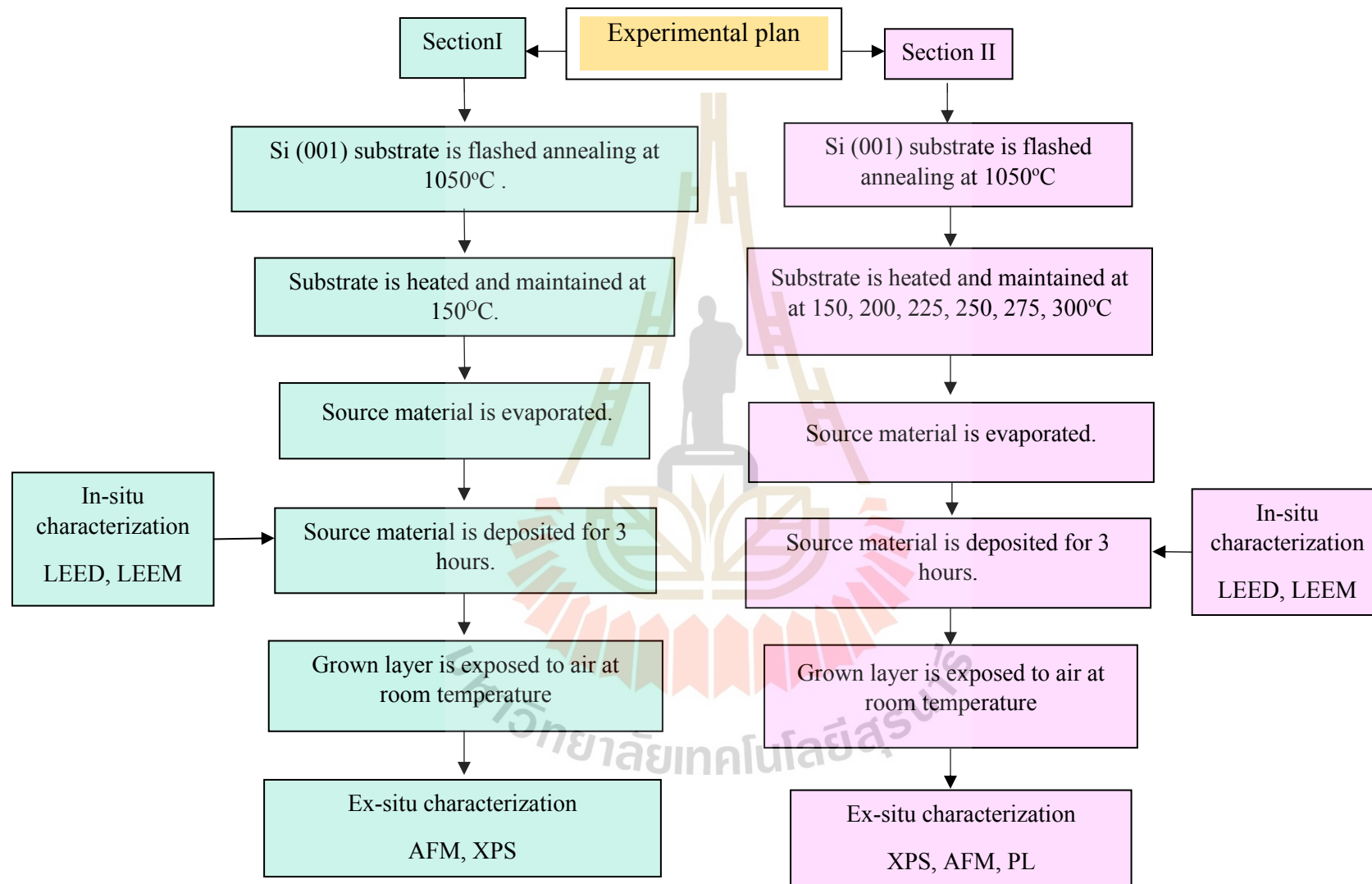


Figure 3.1 Flow charts of the experimental procedure.

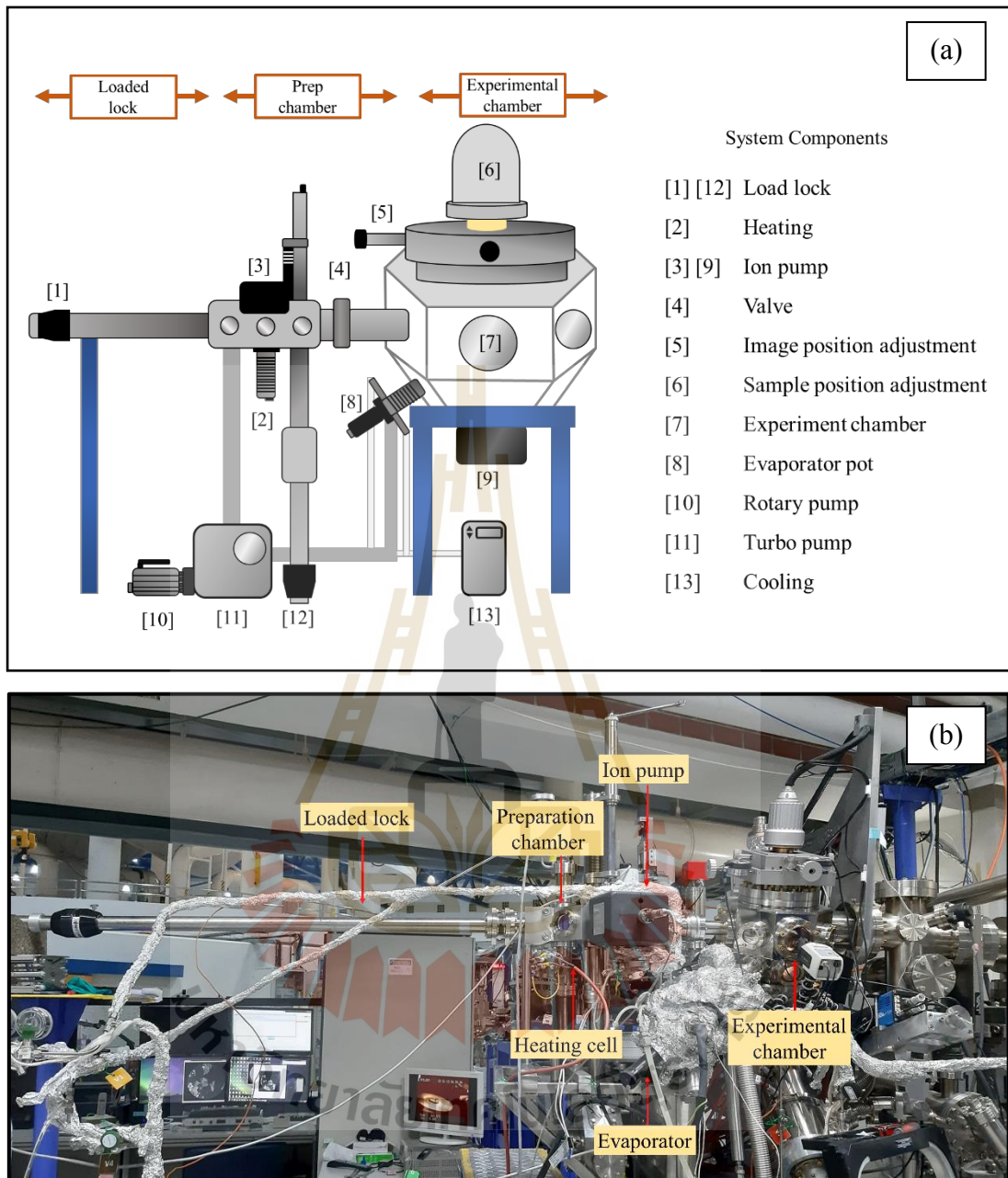


Figure 3.2 (a) Schematic diagram and (b) photograph of the MBE system at BL3.2Ub: PEEM, SLRI, Thailand.

3.3 Preparation of material source and substrate

In this work, Sn metal powder with purity of $> 99.99\%$ (Sigma Aldrich) was used as source material. The source material was prepared as a pellet with the diameter of 6 mm and put into the tungsten crucible of the electron beam evaporator (Tetra series of e-flux evaporator).

Si (001) with the size approximately of $1 \times 1 \text{ cm}^2$ was used as a substrate. The substrate was mounted on the sample heating holder as shown in Figure 3.3. Prior to the growth, the Si substrate was cleaned by flashed annealing at 1050°C . No chemical treatment was performed. The cleanliness and quality of the substrate was checked by LEED. The LEED pattern of the cleaned Si surface show the clear (2x1) (1x2) Si LEED pattern as shown in Figure 3.4.



Figure 3.3 Photograph of the sample holder.

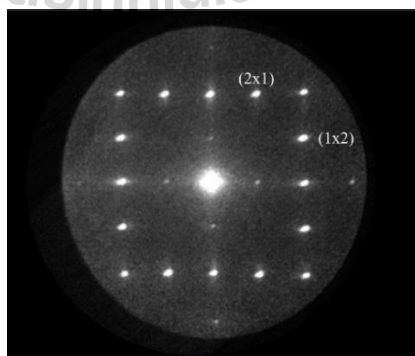


Figure 3.4 LEED pattern of Si (100) substrate after flashed annealing at 1050°C .

3.4 Characterization techniques

3.4.1 Low energy electron microscope (LEEM)

LEEM is a technique that can be used to image atomically clean surface of a material. The schematic diagram of typical LEEM experiment is shown in Figure 3.5. In this technique, a high energy electron beam with energy of between 5-15 eV are focused by electromagnetic lenses and deflected toward the sample surface. The electron beam is then rapidly decelerated before hitting the sample surface to low energy between 0-10 eV. The electrons are then reflected, or diffracted, from the sample surface. The reflected electrons are accelerated again to high energy and their distribution is amplified by several lenses and imaged by a set of channel-plates and then a phosphor screen. LEEM is not a scanning technique. LEEM imaging can be carried out in real-time at video frame rate. It is therefore an ideal instrument for monitoring in situ dynamic processes, such as growth and self-organization of nanostructures and thin films. Lateral resolution of our LEEM is better than 10 nm. LEEM also allows to perform LEED in selected (micrometer sized or even smaller) areas of the surface.

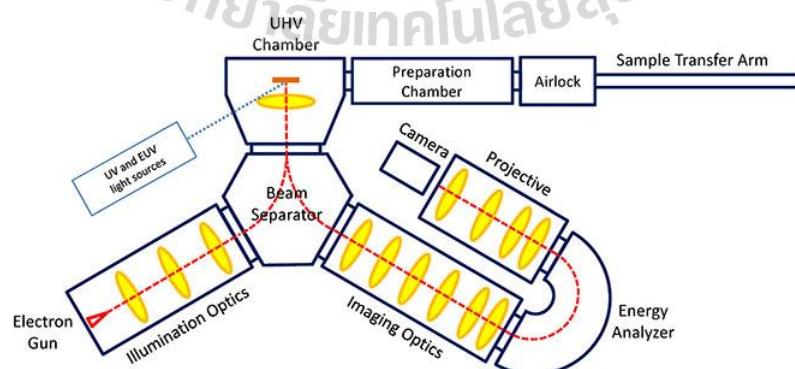


Figure 3.5 Schematic diagram of LEEM experiment (<https://groups.oist.jp/fsu/leem>).

In this work, LEEM was used for real-time monitoring the growth of tin oxide on Si (100) substrate. SPELEEM system (Elmitech's LEEM III) installed at BL 3.2b: PEEM was used in the experiment. The LEEM images were performed within a bias voltage of -20 kV and field of view 50 micrometers.

3.4.2 Low energy electron diffraction (LEED)

LEED is a surface analysis technique that is widely used to study surface structure of a material. In this technique, low energy electrons in the range of 20 to 200 eV which can be considered as a stream of waves are bombarded a sample surface. If the sample surface is a single crystal with well-ordered surface structure, the electrons are diffracted and form a LEED pattern. The low electrons can penetrate to the sample for approximately 10 Å without losing energy as shown in Figure 3.6. LEED is therefore surface sensitive technique, unlike X-ray diffraction.

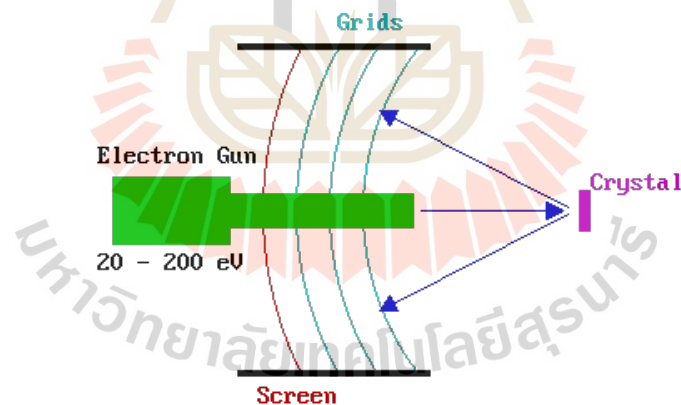


Figure 3.6 Principle of LEED. (R. Wolfgang, 2004)

Electron diffraction follows the Bragg's law as shown in Figure 3.7,

$$n\lambda = a\sin\theta, \quad (3.1)$$

where λ is the wavelength, a is the atomic spacing, θ is the angle between the incident beam and the reflected beam, and n is an integer. The size of the path difference is $a \sin \theta$ and this must be equal to an integral number of the wavelengths for constructive interference to form a pattern at the detector.

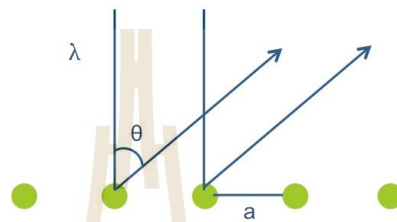


Figure 3.7 Schematic diagram of electron diffraction principle. (R. Wolfgang, 2004)

For example, the LEED pattern from an fcc(110) surface is shown in Figure 3.8. In Figure 3.8, the left diagram shows the atomic structure and the right diagram shows the diffraction pattern. The pattern shows the same rectangular symmetry as the substrate surface, but it is stretched in the opposite sense to the real space structure due to the reciprocal dependence upon the lattice parameter. The observed LEED pattern is a (scaled) representation of the reciprocal net of the pseudo-2D surface structure

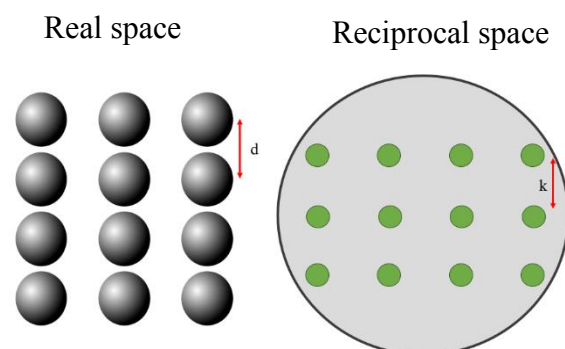


Figure 3.8 Real space and reciprocal space of face center cubic or fcc(110) structure.

The reciprocal net is determined by (defined by) the reciprocal vectors: a_1^* & a_2^* (for the substrate) The reciprocal vectors are related to the real space unit cell vectors: a_1 & a_2 (for the substrate) by the scalar product relations:

$$a_1 \cdot a_2^* = a_1^* \cdot a_2 = 0 \text{ and } a_1 \cdot a_1^* = a_2 \cdot a_2^* = 1 \quad (3.2)$$

These mean that a_1 is perpendicular to a_2^* , and a_2 is perpendicular to a_1^* . There is an inverse relationship between the lengths of a_1 and a_1^* (and a_2 and a_2^*) of the form:

$$|a_1| = 1 / (|a_1^*| \cos A), \quad (3.3)$$

where A is the angle between the vectors a_1 and a_1^* . when $A = 0$ degrees ($\cos A = 1$) this simplifies to a simple reciprocal relationship between the lengths a_1 and a_1^* .

As shown in Figure 3.9, for example, the diagram below shows an fcc (100) surface (again in plan view) and its corresponding diffraction pattern (i.e. the reciprocal net).

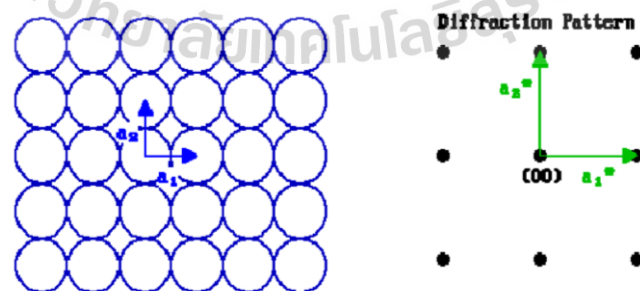


Figure 3.9 Atomic structure and diffraction pattern of fcc(100) a_1^* must be perpendicular to a_2 and a_1^* is parallel to a_1 , the angle between a_1 and a_1^* is zero, so $|a_1| = 1 / |a_1^*|$. (R. Nix., 2019) (R. Wolfgang, 2004).

In this work, LEED was used for real-time monitoring the growth mechanism. This technique was performed on SPELEEM system (Elmitech's LEEM III) installed at BL 3.2b: PEEM, SLRI.

3.4.3 Atomic force microscopy (AFM)

AFM is the most versatile and powerful microscopy technique for studying a surface at the nanoscale. This technique can image in three-dimensional topography (x, y, and z) and identifies the type of surface measurement. In this technique, a very sharp tip attached to a cantilever is scanned over a sample surface to sense surface force. The curly cantilever will change while the tip was scan over a different surface (smooth, roughness). The cantilever deflections away from the surface is detected by reflecting an incident laser beam which is detected a photodetector as shown in Figure 3.10. AFM images or the topography is generated by the interaction force between tip and sample surface (shown in Figure 3.10) which relate with the Hook's law

$$F = -kx, \quad (3.3)$$

when F is the force acting on the cantilever, k is the cantilever spring constant and x is the vertical displacement of the end of the cantilever

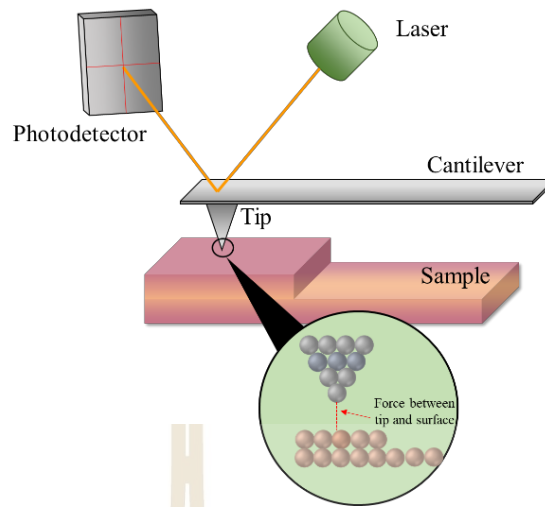


Figure 3.10 Schematic diagram of AFM experiment.

AFM can be divided by the force between tip and surface as contact, non-contact mode, and tapping mode.

1. Contact mode: Tip touches the sample surface with the constant force. The contact mode measures the repulsion between tip and sample.
2. Non-contact mode: Tip does not touch the sample surface. The non-contact mode measures the Van der Waals forces between tip and sample detected
3. Trapping tapping mode: Tip vertically oscillates between contacting sample surface and lifting of at frequency of 50,000 to 500,000 cycles/sec.

AFM can also measure the surface current and potential which is called the conductive atomic force microscopy (C-AFM). C-AFM can simultaneously measure topography and current over the sample surface by using a conductive tip as a nanometer-scale electrical probe. The cantilever and tip will measure with the constant height from the surface and constant bias voltage between tip and surface as shown in Figure 3.11.

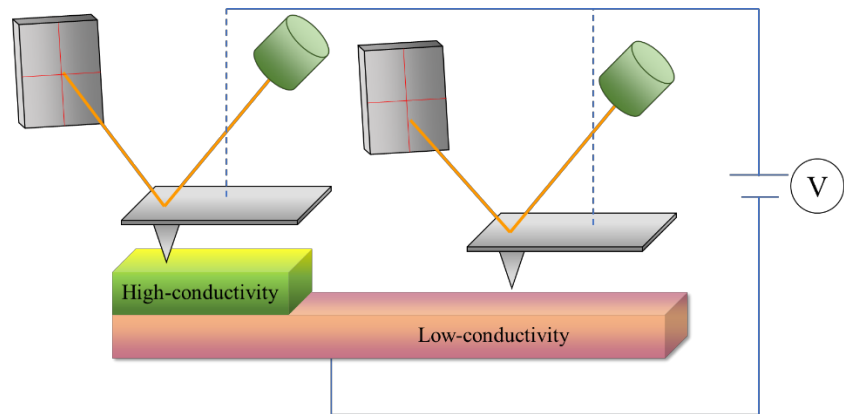


Figure 3.11 Schematic diagram of C-AFM measurement.

Besides, AFM is also developed for measuring the electrical properties on the surface which is called the electrostatic force microscopy (EFM). EFM applies a voltage between a tip and sample while the tip scan above the surface. The different charges (negative or positive) will affect the deflection of the cantilever as shown in Figure 3.12. Therefore, EFM contains information such as surface potential and charge distribution on the sample surface.

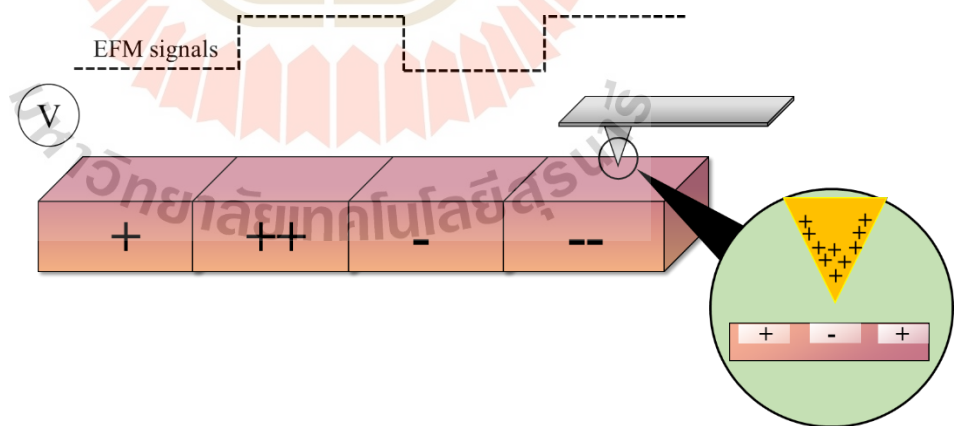


Figure 3.12 Schematic diagram of EFM measurement.

In this work, AFM was performed on Park Systems AFM XE-120 at the center for scientific and technological equipment, Suranaree university of technology. It was used to study the morphology, size, shape of the grown SnO₂ samples. The measurements were carried out in the area of 5x5 μm² with a scan rate frequency of 0.25 Hz in non-contact atomic force microscope mode.

C-AFM was used to measure current distribution (conductivity) over the sample surface. The Si coated gold was used as the tip. The bias voltage between tip and sample is 10V and the scan rate frequency is 0.5 Hz within I-AFM mode.

EFM was used to study the surface potential of the sample with bias voltage of 10V and a scan rate frequency of 0.5 Hz. The AFM, C-AFM, and EFM results were analyzed by the XEI program, version 4.3.0 build5.

3.4.4 X-ray Photoelectron spectroscopy (XPS)

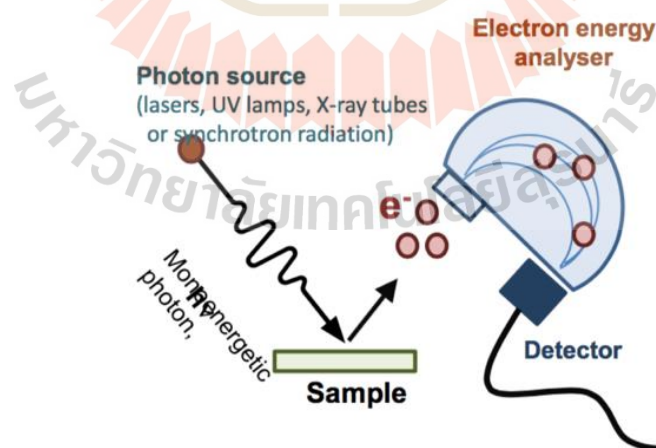


Figure 3.13. Schematic diagram of XPS experiment.

XPS is a powerful technique used to study the chemical composition of the sample. This technique is very surface sensitive that has the analysis depth of about 1-10 nm. This technique is based on the photoelectric effect. In this technique, a sample surface is irradiated with a monoenergetic X-ray beam. The X-rays are adsorbed by surface atoms and their core electrons are ejected from the surface. This process is schematically shown in Figure 3.13. The photo-emitted electrons are detected, and their kinetic energies are measured using electron energy analyzer. The kinetic energy of the photo-emitted electrons (E_{kin}) is related to the binding energy of electron (E_B) in the following equations 3.4:

$$E_{kin} = hv - E_B - \phi, \quad (3.4)$$

where, hv is the energy of photon source (X-ray) and ϕ is the spectrometer work function. As the energy of X-ray and the spectrometer work function are known, the binding energy of the photo-emitted electrons can be simply calculated. The binding energies of core level electrons are unique for each chemical species.

The surface chemical composition of the grown SnO₂ samples was confirmed by XPS technique. The measurements were carried out at BL5.3: SUT-NANOTEC-SLRI XPS and BL3.2Ub: PEEM, SLRI., The XPS measurement at BL5.3: SUT-NANOTEC-SLRI XPS was performed on the PHI5000 VersProbeII (Japan) The Al K α 1486.6 eV radiation was used as an excitation source

The emitted photoelectron was recorded using a hemispherical electron energy analyzer at the pass energy of 117.4 eV and 46.95 eV for the survey spectrum and high-resolution spectra, respectively. The spectra were collected with step energy of 0.05 eV and time per step of 20 ms. The high-resolution spectra results were deconvoluted with PHI Multi Pak XPS software. The relative atomic concentration of element was calculated using Equation 3.5.

$$\text{Atomic concentration} = \frac{\frac{I_x}{S_x \times T_x}}{\sum_{i=1}^n \frac{I_i}{S_i \times T_i}}, \quad (3.5)$$

where, I is the intensity or area peak, S is the sensitivity factor and, T is the time per second (From measured parameter)

The measurement at BL3.2Ub: PEEM used the synchrotron light as X-ray source. The energy of the x-ray source was fixed at 650 eV. The spectra were collected with step energy of 0.2 eV and time per step of 2 seconds.

3.4.5 Photoluminescence spectroscopy (PL)

PL is a powerful technique for studying optical properties and electronic structure of materials. When samples or materials are excited by light which renders absorption and imparts excess energy into the materials in a process called “Photo-excitation”. The excess energy can be dissipated from the sample by radiative process or luminescence. Therefore, the photoluminescence is the spontaneous emission of light from materials under optical excitation.

The radiative process of the semiconductor materials is defined with the energy difference of the valence band and conduction band which is well known as the

“bandgap”. When the laser light is directed onto the sample with energy much larger than the optical bandgap. The electrons from the equilibrium state or valence band are excited and moved to the conduction band. These electrons do not stable in the conduction band which leads to recombined on the valence band or radiative transition. Besides, the radiative transition of the semiconductor may also involve defected in the structure or impurity levels as shown in Figure 3.14 which relates to emission length and the spectra.

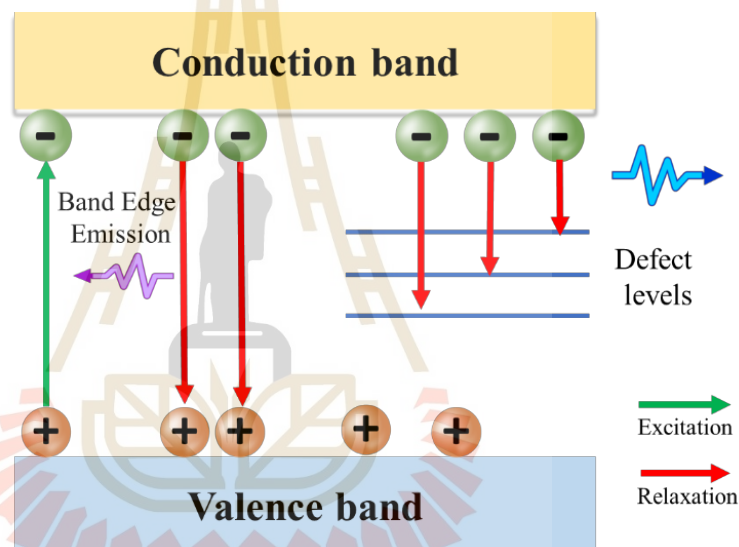


Figure 3.14 Principle of photoluminescence.

The information of PL contains the characteristic spectrum which can identify the defect of the structure and impurities, and the magnitude of PL spectra allows determining their concentration.

The typical PL setup is shown in Figure 3.15. The excitation wavelength is selected by the excitation monochromator which contains the mono wavelength (λ excitation). After the exciting wavelength through the sample. The luminescence is

observed through a second monochromator and detector, an emission spectrum is produced.

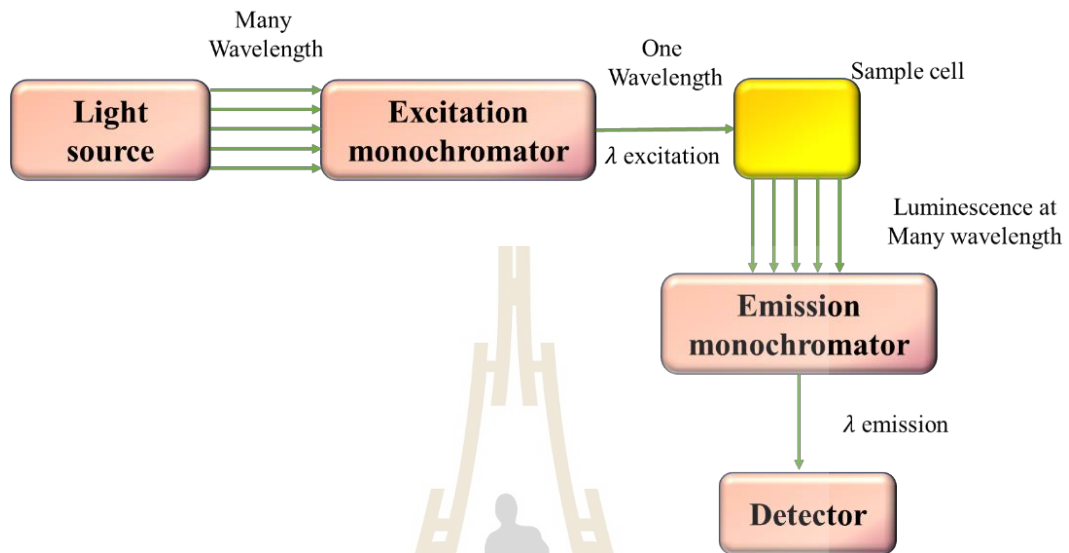


Figure 3.15 Schematic of photoluminescence experiment.

In this work, the optical property was characterized by PL. The PL measurement was performed by Horiba Jobin YVON, FluoroMax-4, Japan at National metal and materials technology center (MTEC), NSTDA, Thailand. The sample was excited with the wavelength of 350 nm and the spectra were collected in an emission range of 440 to 600 nm with step of 0.5 nm. The PL results was fitted with the fitting function on the Magicplot program using the linear for background subtract.

CHAPTER IV

RESULTS AND DISCUSSION

This chapter presents the experimental results which are divided into two parts. In the first part, the growth mechanism was real-time studied by in-situ LEED and LEEM and the grown SnO₂ layer was characterized by XPS and AFM. In the second part, the effect of substrate temperature on the growth was studied. The growth at different substrate temperatures was monitored by in-situ LEED. The grown SnO₂ layers were characterized by XPS and AFM and their optical properties were investigated by PL.

4.1 Study on the growth mechanism

In this experiment, the Si (100) substrate with the size of 1x1 cm² was cleaned by flashed-anneal at 1050°C for 5 times. Sn was firstly deposited onto to the substrate by evaporating Sn powder at the temperature of approximately 1000°C. The parameters for the evaporator are as follows, high voltage: 1 kV, emission current: 12 mA, filament current: 6.5 A, and flux current: 50 nA. During the deposition, the substrate was heated and maintained at the temperature of 150°C. The deposition was real-time monitored by in-situ LEED and LEEM. The deposition was carried out for 180 minutes under the pressure of less than 5x10⁻⁹ mbar. After the deposition, the deposition sample was exposed to air at room temperature for 15 minutes. The growth process was then complete. The grown sample was consequently characterized by XPS and AFM.

4.1.1 Low energy electron diffraction (LEED)

LEED pattern of the Si (100) substrate prior to the deposition is shown in Figure 4.1(a). The LEED pattern showed the clear (1x2) and (2x1) patterns indicating the clean and well-ordered surface of Si (100) substrate after flashed annealing at 1050°C. It is noted that no chemical etching or treatment was made on the substrate before flashed annealing. After the deposition of 60 minutes, the intensity of the LEED patterns decreased as shown in Figure 4.2(b). After the deposition of 120 minutes, the intensity of (1x2) and (2x1) patterns were faded (Figure 4.2(c)). After the deposition of 180 minutes, only the (1x1) pattern was still observed as shown in Figure 4.2(d). This result suggests that tin layer was deposited on the Si substrate, however, the deposited layer may not entirely cover the substrate surface and the LEED pattern of this deposited layer was not observed.

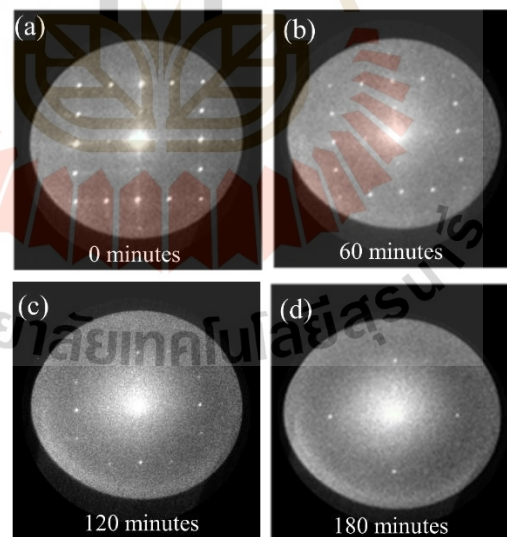


Figure 4.1 LEED patterns of (a) the Si (100) substrate before the deposition (after flashed annealing at 1050°C) and after the deposition of (b) 60, (c) 120 and (d) 180 minutes.

4.1.2 Low energy electron microscope (LEEM)

LEEM images of the Si (100) substrate before the deposition (after flashed annealing at 1050°C) and during the deposition are shown in Figure 4.2. Clean and smooth surface of Si (100) substrate was observed before the deposition. After the deposition of 60 minutes, small particles were observed and distributed over the surface. The density of the small particle increased with the deposition time and the formation of cluster or island was observed. The diameter of the cluster was estimated to be approximately 100 nm. This result suggests that there is a layer which has cluster or island structure deposited on the surface.

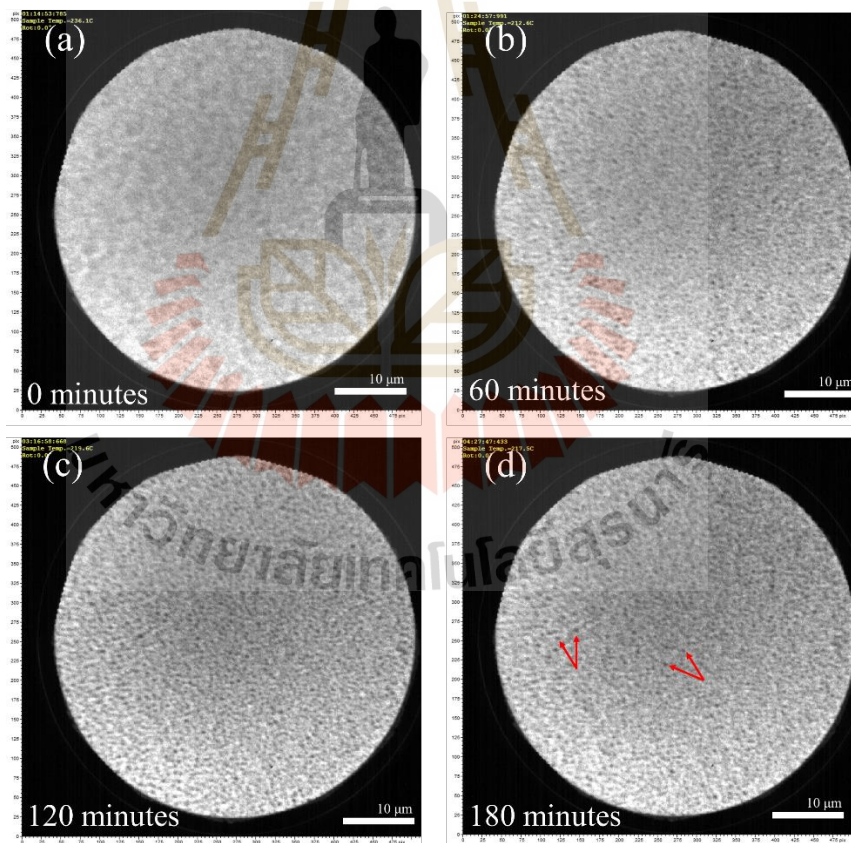


Figure 4.2 LEEM images (Field of view = 50 μm) of (a) the Si (100) substrate before the deposition (after flashed annealing at 1050°C) and after deposition of (b) 60, (c) 120 and (d) 180 minutes.

4.1.3 X-ray photoelectron spectroscopy (XPS)

After the deposition, the sample was exposed to air at room temperature for 15 min for dry oxidation. The chemical composition of the grown sample was investigated by XPS. The survey XPS spectrum of the grown sample is shown in Figure 4.3. The survey spectrum reveals the presences of Sn, O, Si, C on the surface. The high-resolution spectra of Sn3d and O1s peaks are shown in Figure 4.4. The Sn3d_{3/2} peak can be deconvoluted into two main components at the binding energies of 485.3 eV and 486.9 eV which are attributed to Sn metal (Sn-Sn) and Sn dioxide (SnO₂), respectively (Y. H. Kim et al., 2019). The O1s peak can be fitted into two peaks at the binding energies of 531.69 eV and 532.93 eV which are assigned to Sn-O and Si-O, respectively (M. Kwoka et al., 2005). The calculated relative atomic concentration of element is summarized in Table 4.1. The analysis of Sn3d and O1s peak confirms that SnO₂ was successfully grown on the Si (100) substrate. However, the observation of Sn metal indicates that the deposited Sn layer was not fully oxidized after exposure to air at room temperature for 15 m. The estimated atomic content between Sn metal and Sn oxide is 9:1. The analysis depth of XPS is typically in the order of 5-10 nm. In addition, the detection of Si-O suggests that Sn layer did not entirely cover the Si substrate after the deposition. This is consistent with the observation by LEED and LEEM. It is noted that the presence of C on the surface is possibly due to surface contamination after the air exposure.

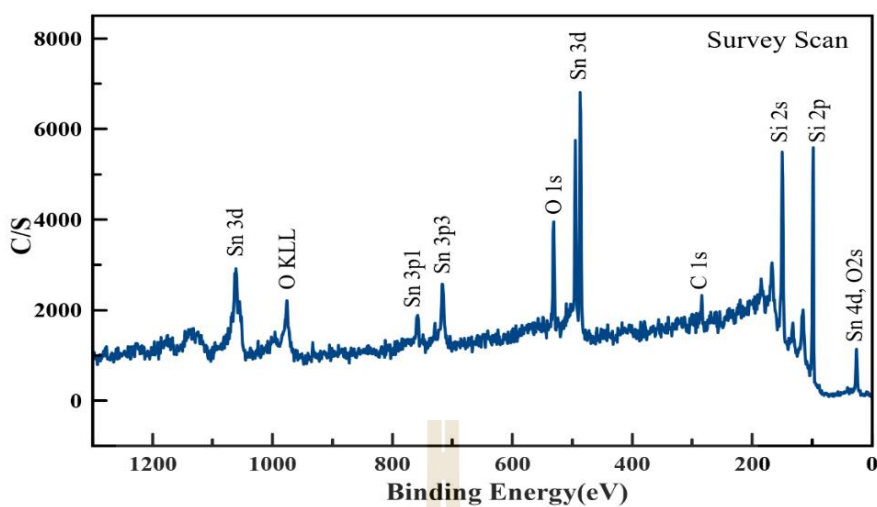


Figure 4.3. Survey XPS spectrum of the grown sample.

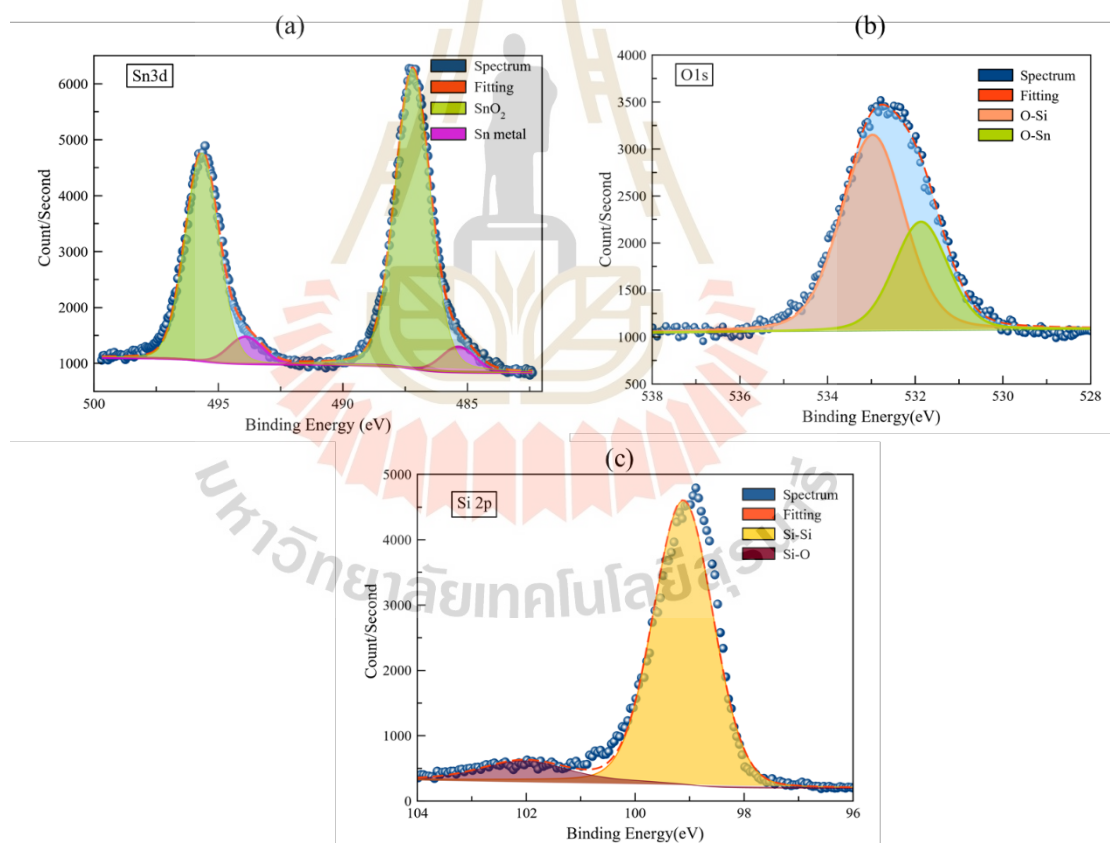


Figure 4.4 High resolution XPS spectra with the deconvolution of (a) Sn 3d and (b) O 1s (c) Si 2p peaks of the grown sample.

Table 4.1 Relative atomic concentration of element of the grown sample calculated from XPS spectra.

Relative atomic concentration (%)			
Sn	O	Si	C
7.69	21.97	55.73	14.61

4.1.4 Atomic force microscopy (AFM)

AFM was used to study the surface morphology and structure of the grown sample. Top view and 3-dimensional AFM images of the grown sample are shown Figure 4.5. The AFM images show the formation of three-dimensional clusters or islands of the grown layer on the surface. The observed clusters have the average diameter and height of approximately 100 ± 10 nm and 6 nm, respectively, and the surface coverage estimated by the ImageJ software is approximately 20%. The details of the surface coverage estimation is given in Appendix A. This result suggests that the growth follows the Volmer-Werber island or Stranki-Krastanov growth mode. This is because the Sn atoms strongly bond with themselves rather than with Si (001) substrate and there is a large compressive strain due to highly mismatched between grown layer and substrate (lattice mismatch of 9%).

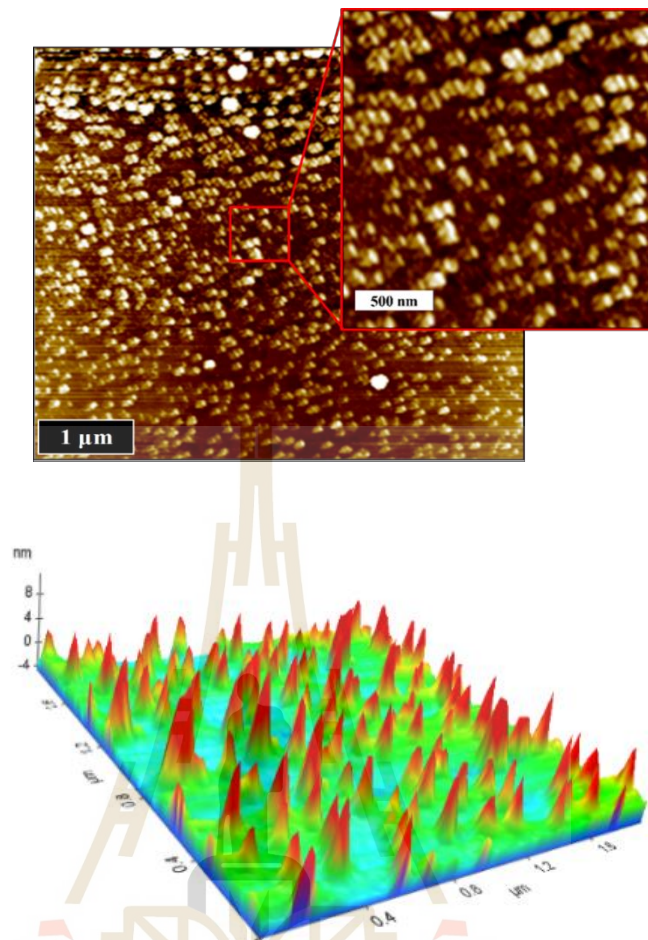


Figure 4.5 Top view and 3-dimensional AFM images of the grown sample.

4.1.5 Conductive atomic force microscopy (C-AFM) and Electrostatic force microscopy (ESM)

The surface morphology and nanostructure of the grown sample was further investigated by C-AFM and ESM. Figure 4.6 shows the topographic image and current profile in the selected area obtained from the C-AFM measurement. Two different levels of current profiles were observed. The high current of approximately 25 pA was measured in the area of clusters corresponding to the cluster size of approximately 100 nm. No current in the area between the clusters was detected. This result is consistent

with the ESM measurement that the surface potential of approximately 1 mV was measured only in the cluster regions as shown in Figure 4.7. The detection of high surface current and potential in the cluster area is due to the presence of Si metal of the grown layer as detected from the XPS. This result confirms that the grown layer does not entirely cover the surface but forms the cluster or island structure on the surface.

The growth mechanism and chemical composition results indicate that SnO_2 has successfully grown on Si (100) substrate and appeared as the quantum dots.

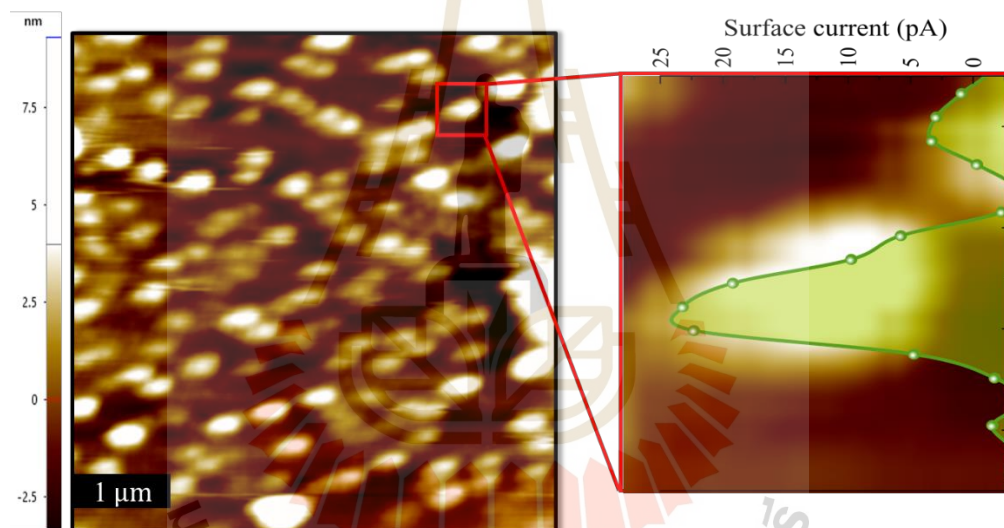


Figure 4.6 Topographic image of the grown sample and current profile in the cluster region (inset) obtained from the C-AFM measurement.

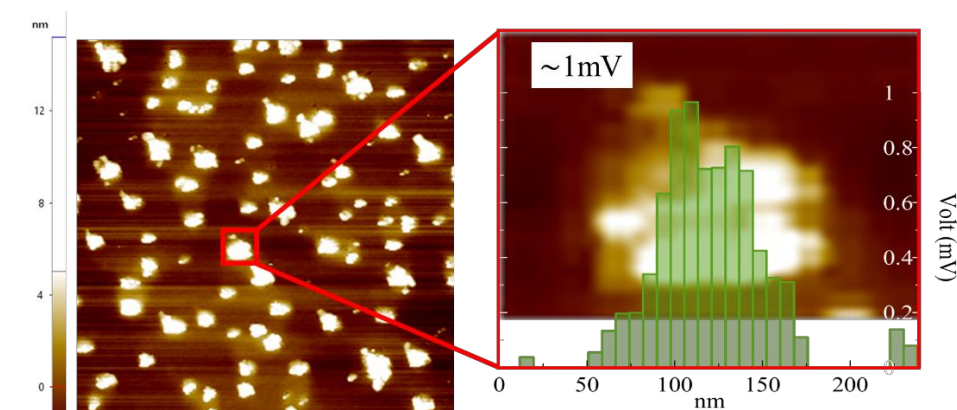


Figure 4.7 Topographic image of the grown sample and the potential profile in the cluster region (inset) obtained from the EFM measurement.

4.2 Study on the effect of substrate temperature on the growth

To study the effect of substrate temperature, the growths of SnO_2 at different substrate temperatures were carried out in a similar manner to section 4.1. The substrate temperatures (ST) were varied from 150, 200, 225, 250, 275 and 300°C and the corresponding grown samples were labelled as ST-150, ST-200, ST-225, ST-250, ST-275 and ST-300, respectively. The growths were real-time monitored by in-situ LEED. The chemical composition and surface morphology of the grown samples were studied by XPS and AFM. In addition, the optical properties of the grown samples were investigated by PL.

4.2.1 Low energy electron diffraction (LEED)

LEED pattern during the Sn deposition at the different substrate temperatures are shown in Figure 4.8. The intensity of LEED patterns of all samples decreased with the deposition time and

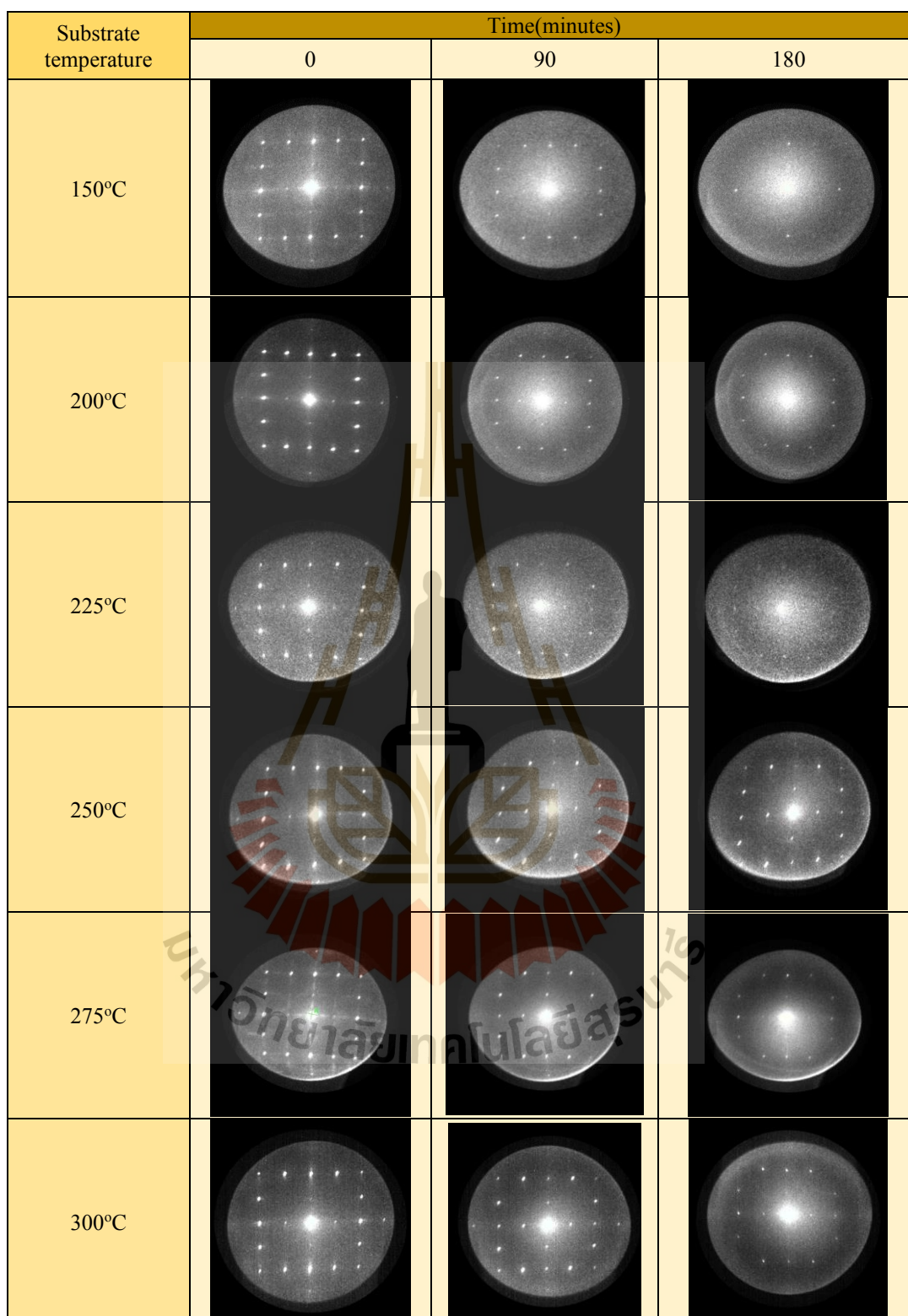


Figure 4.8 LEED patterns during the deposition at different substrate temperatures.

(1x1) pattern was still observed after the deposition of 180 minutes. This result suggests that the deposition layer did not entirely cover the Si (100) substrate and the clusters of deposited layers may be formed at all the substrate temperatures.

4.2.2 X-ray photoelectron spectroscopy (XPS)

The survey XPS spectra of the samples grown at different temperatures are shown in Figure 4.9. The survey spectra of all samples reveal the presences of Sn, O, Si, and C. The presence of C on the surface is due to surface contamination. The calculated relative atomic concentrations of elements are listed in Table 4.2. The highest Sn content was observed on the sample grown at the substrate temperature of 225°C (ST-225).

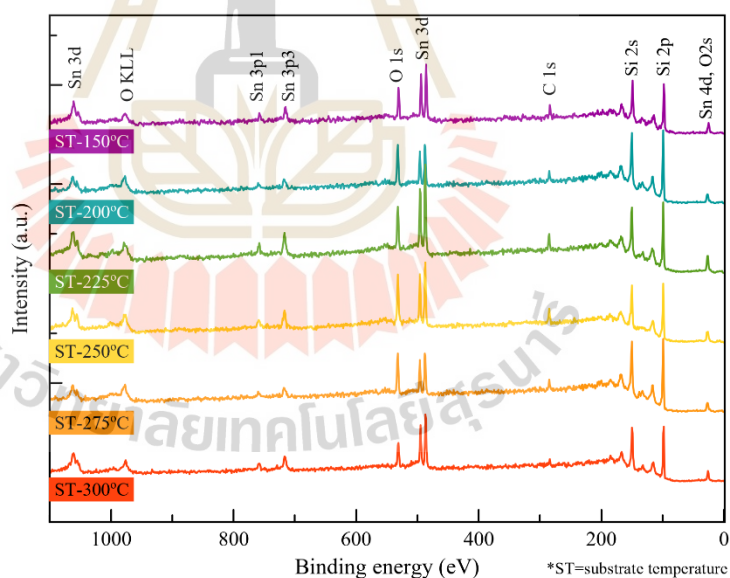


Figure 4.9 Survey XPS spectra of the grown samples ST-150, ST-200, ST-225, ST-250, ST-275, and ST-300.

Table 4.2 Relative atomic concentration of Sn compared with Si of the grown sample calculated from XPS spectra.

Relative atomic concentration of each element compared with Si						
	ST-150	ST-200	ST-225	ST-250	ST-275	ST-300
Sn	10.87%	8.50%	11.27%	9.28%	8.39%	7.45%
O	29.11%	33.88%	35.62%	28.65%	25.27%	21.21%
C	25.51%	29.66%	23.46%	21.51%	12.48%	12.09%

High-resolution spectra of Sn 3d peaks of the sample grown at different temperatures are shown in Figure 4.10. The Sn3d peaks of all samples can be deconvoluted into two components at the binding energies of 485.3 eV and 486.9 eV which are attributed to Sn metal (Sn-Sn) and tin dioxide (SnO₂), respectively (Y. H. Kim et al., 2019).

Table 4.3 Percentage of metallic tin and tin dioxide of the grown samples calculated from XPS spectra.

Sample	%Metallic Tin	%Tin Dioxide
ST-150	7.16	92.84
ST-200	8.73	91.27
ST-225	7.90	92.10
ST-250	5.87	94.13
ST-275	14.21	85.78
ST-300	33.18	66.82

The estimated atomic content between Sn metal and Sn oxide are for the sample ST-150, ST-200, ST-225, ST-250, ST-275, and ST-300 was showed in Table 4.3.

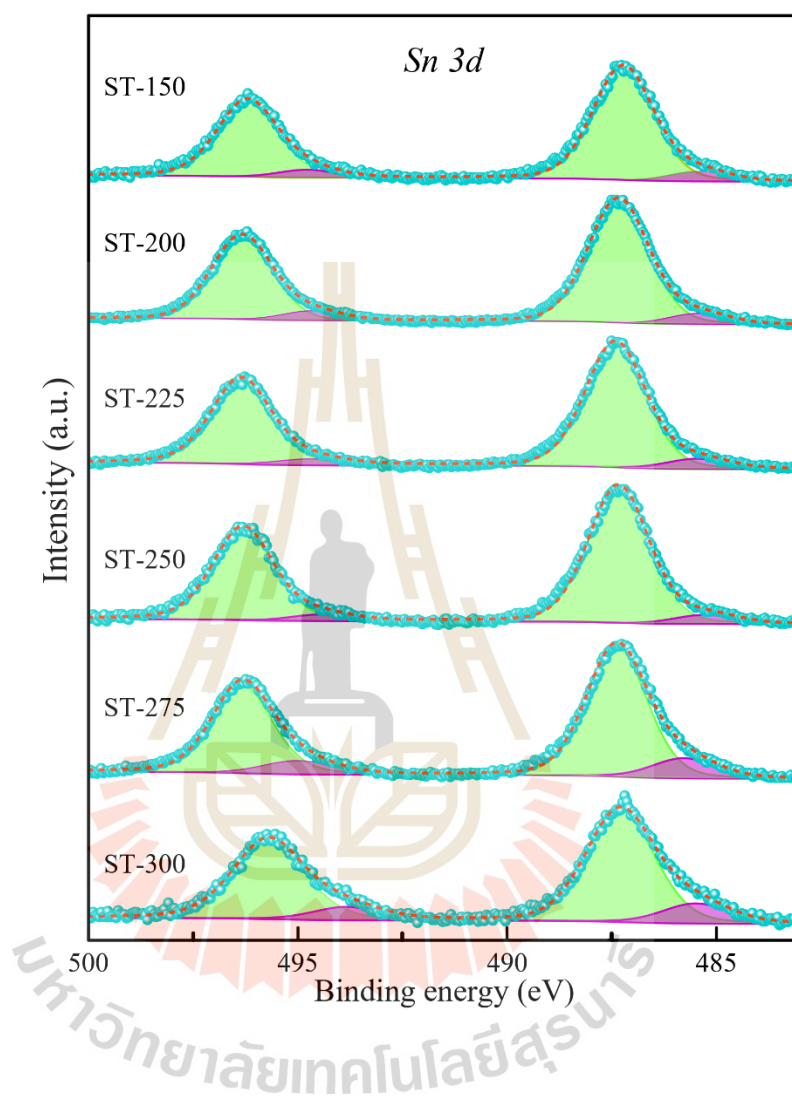


Figure 4.10 High-resolution XPS spectra of Sn 3d peaks of the grown samples ST-150, ST-200, ST-225, ST-250, ST-275, and ST-300.

The XPS result suggests that the substrate temperature do not significantly affect the chemical composition of the grown.

4.2.3 Atomic force microscope (AFM)

AFM top view images of the samples grown at different substrate temperatures are shown in Figure 4.11. The formation of cluster or island of the grown layer was observed in all samples. The average diameters of cluster are 127.7, 98.3, 86.9, 87.1, 111.6, and 124.0 nm for the sample ST-150, ST-200, ST-225, ST-250, ST-275, and ST-300, respectively. The plot between the average quantum dot size and substrate temperature is also shown blue line in Figure 4.13.

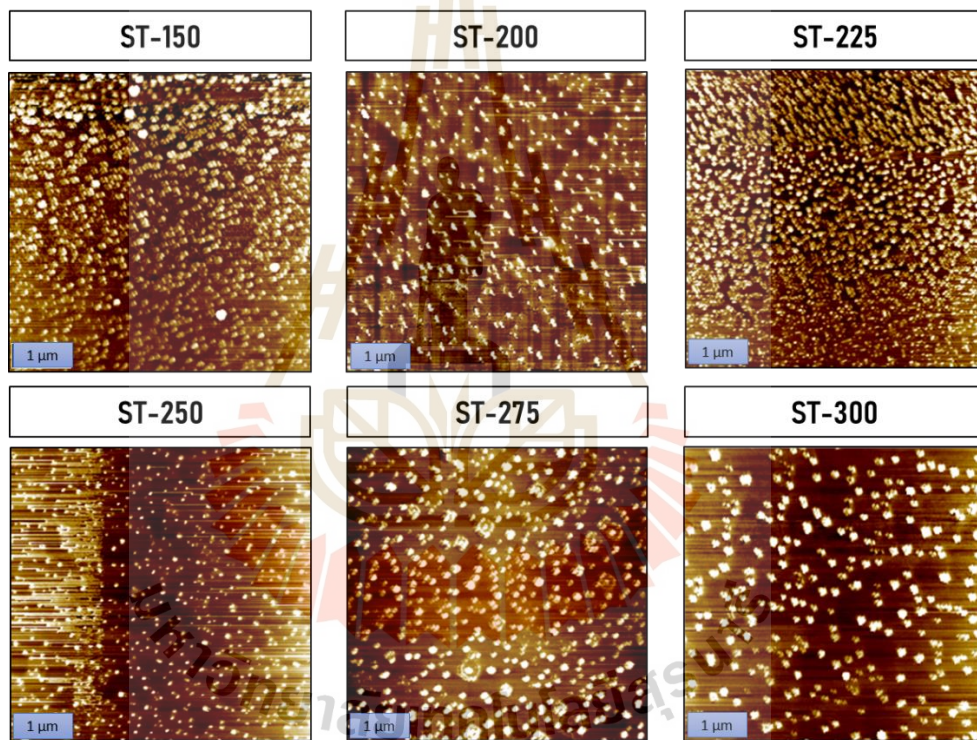


Figure 4.11 AFM top view images of the samples grown at different substrate temperatures.

We found that the size of the quantum dot is related to the atomic percentage of the metallic tin (as shown red line in figure 4.12) which demonstrates as the quantum dot smaller they become more oxidized.

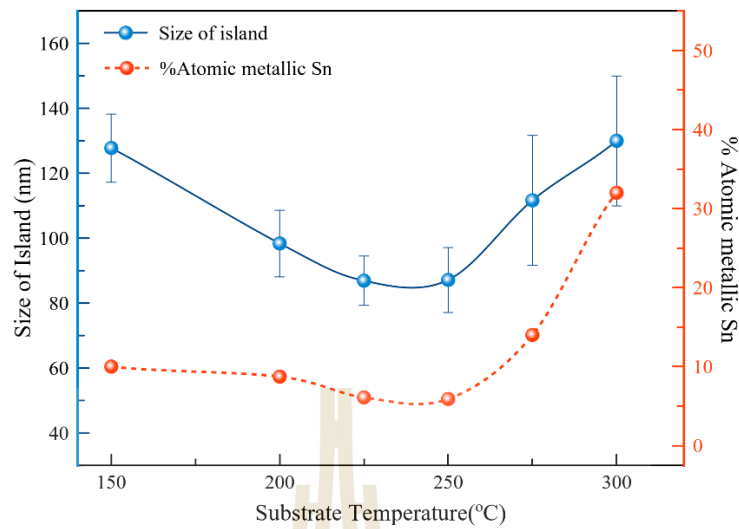


Figure 4.12 the relation between the average size of the quantum dot, the atomic concentration of metallic tin, and substrate temperatures.

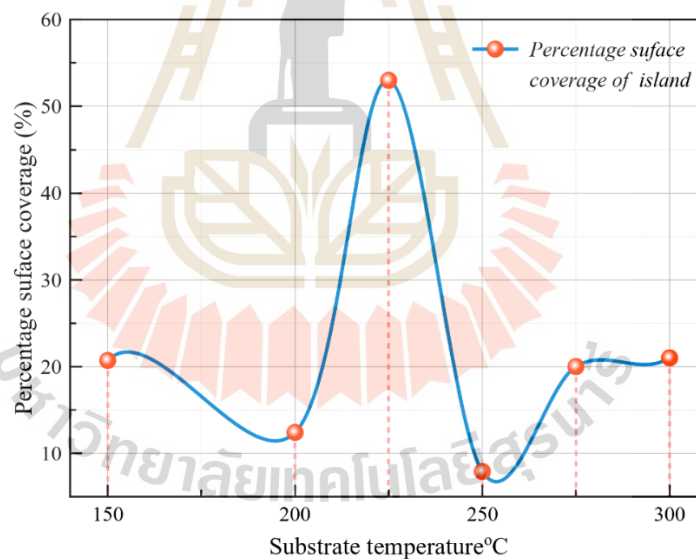


Figure 4.13 Plot between the surface coverage of the cluster on the Si substrate and substrate temperatures.

The surface coverages calculated from the ImageJ software were found to be 20.7%, 12.4%, 53%, 7.9%, 20%, and 21% for the sample ST-150, ST-200, ST-225, ST-250, ST-275 and ST-300 respectively. The plot between the surface coverage and

substrate temperatures is also shown in Figure 4.13. The smallest average of cluster size of 86.9 ± 10 nm and the highest surface coverage of 53% were observed on the sample grown at the substrate temperature of 225 °C. This result is consistent with the change of LEED pattern during the deposition.

3-dimensional AFM images of the samples grown at different substrate temperatures are shown in Figure 4.14. It was observed that the grown layers of the samples grown at the substrate temperature between 150 °C to 275 °C have a cone-shaped structure with a height of approximately 6 nm. This result suggests that the growth follows the Volmer-Werber island or Stranki-Krastanov growth mode.

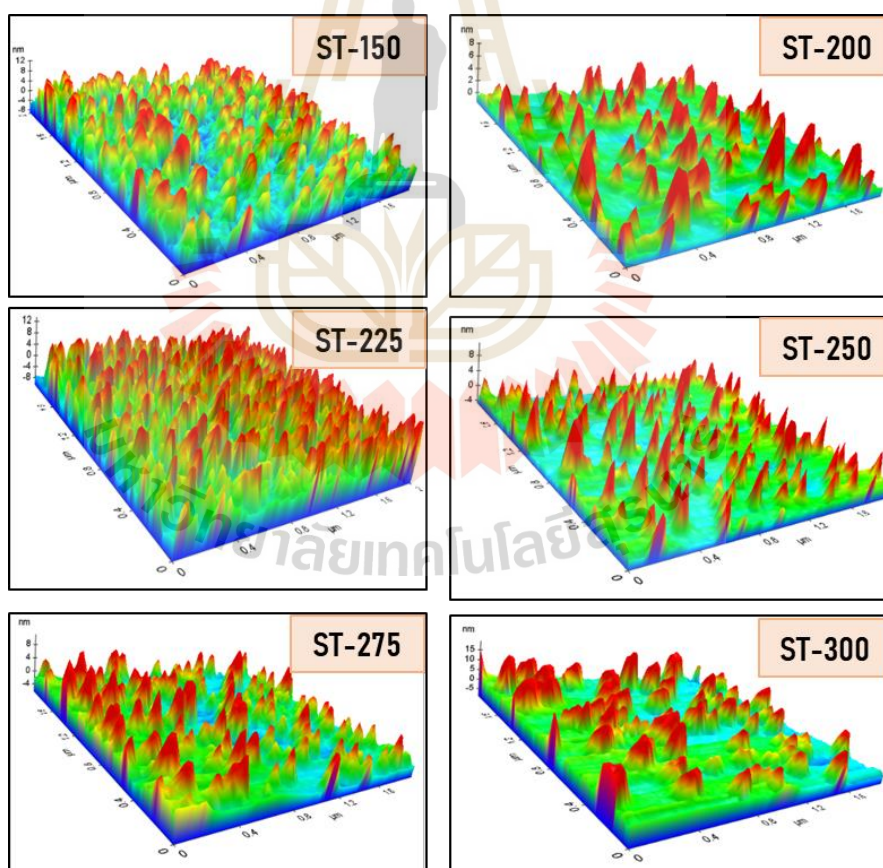


Figure 4.14 3-dimensional AFM images of the grown sample ST-150, ST-200, ST-225, ST-250, ST-275 and ST-300.

4.2.4 Photoluminescence spectroscopy (PL)

The optical properties of the samples are also studied by PL. The PL spectra were collected at room temperature in the emission range of 430-500 nm with an excited wavelength of 350 nm. The subtracted background PL spectra of all samples are shown in Figure 4.15. Generally, the photoluminescence of SnO₂ is observed in the range 350-550 nm (UV and visible region both) (A. Kar et al., 2011). SnO₂ nanocrystals with large size and nearly perfect crystalline structure generally show stronger UV emission assigning to their perfect band edge emission (A. Kar et al., 2011) (M. L. Fileyska et al., 2018). In this work, all the samples show the same dominant photoluminescence in the blue region (~440 - 490 nm).

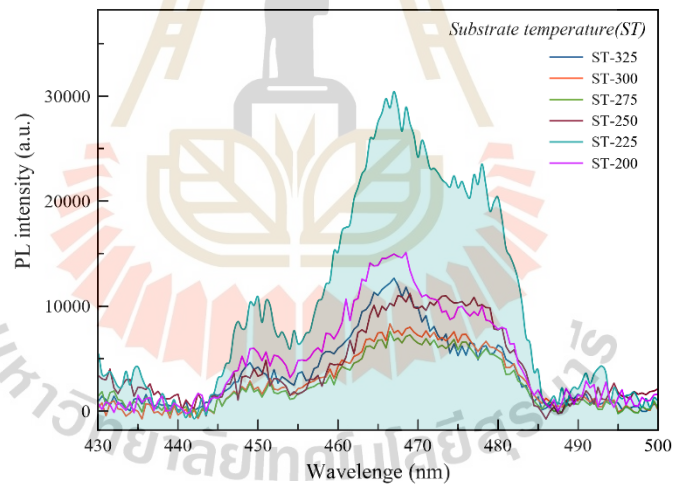


Figure 4.15 PL emission spectra of the grown samples ST-150, ST-200, ST-225, ST-250, ST-275 and ST-300.

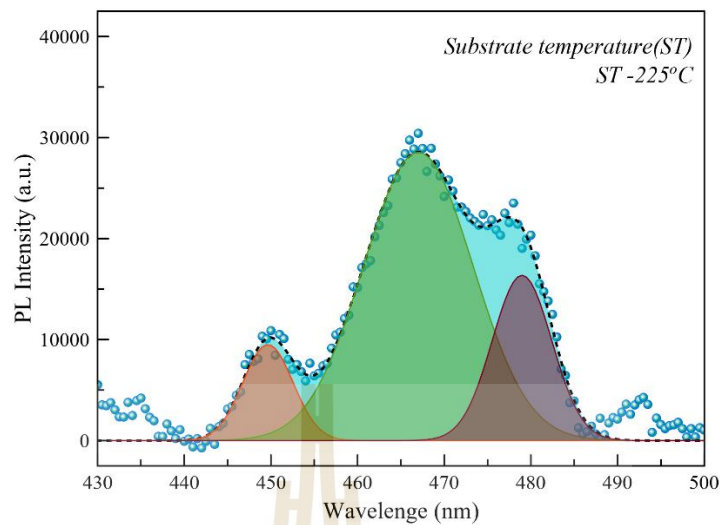


Figure 4.16 Deconvolution of the PL emission spectrum of the ST-225 sample.

The deconvolution of the PL peak of the ST-225 sample shown in Figure 4.16 reveals three PL peaks at peaks at λ 450 (2.76 eV), 467 (2.66 eV), and 478 (2.60 eV) nm. These values are lower than the bandgap of SnO₂ of about 4.37 eV.

It is believed that these emissions are originated from the level of the defect in the bandgap, like oxygen. Usually, oxygen vacancies are the most common defects and frequently act as radioactive centers in luminescence methods (ET. Selvi et al., 2017)

In the lattice of SnO₂, the O²⁻ ions can evade from the lattice which brings about to the formation of oxygen vacancies or defect levels. The oxygen vacancy (V_0) center can trap an electron which leads to the formation of V_0^* state. The model of energy level consists of three consequents as the valence band, defect level (V_0^*/V_0^{**}), and conduction band as shown in Figure 4.17. The luminescence mechanism starts from the creation a positive hole and the negative electron in the valence band by excitation. Thereafter, the relaxation process can occur with the hole in the valence band trapped at the V_0 a site which brings about to the V_0^* defect level. This surface traps hole tunnels back into

the film to recombine with an electron in the deep trap V_o^* center leading to the formation of V_o^{**} center at the surface of the island as shown in Equation (4.1).



Thereafter, the V_o^{**} center recombined with an electron in the conduction band which leads to trap emission in visible blue light as shown in Figure 4.18 and Equation 8.

(A. Kar et al., 2011) (S. Sharma et al., 2012)

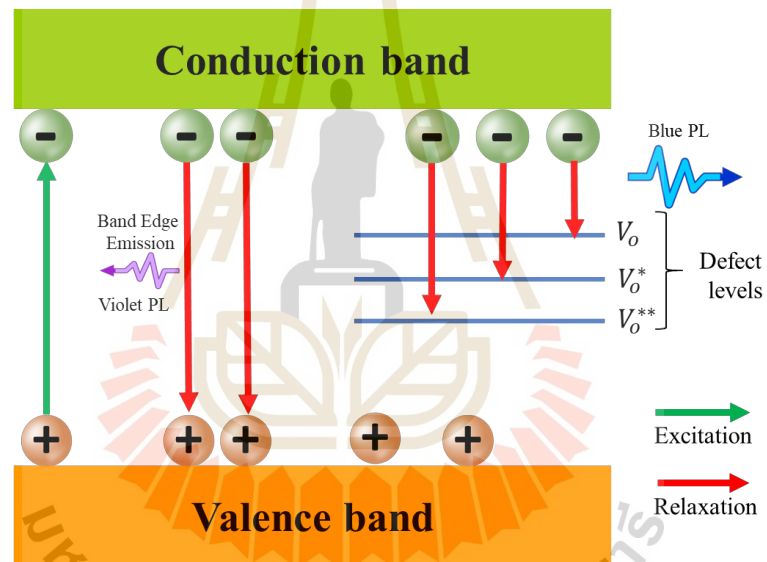


Figure 4.17 Schematic Model for different relaxation process in SnO₂

CHAPTER V

CONCLUSION

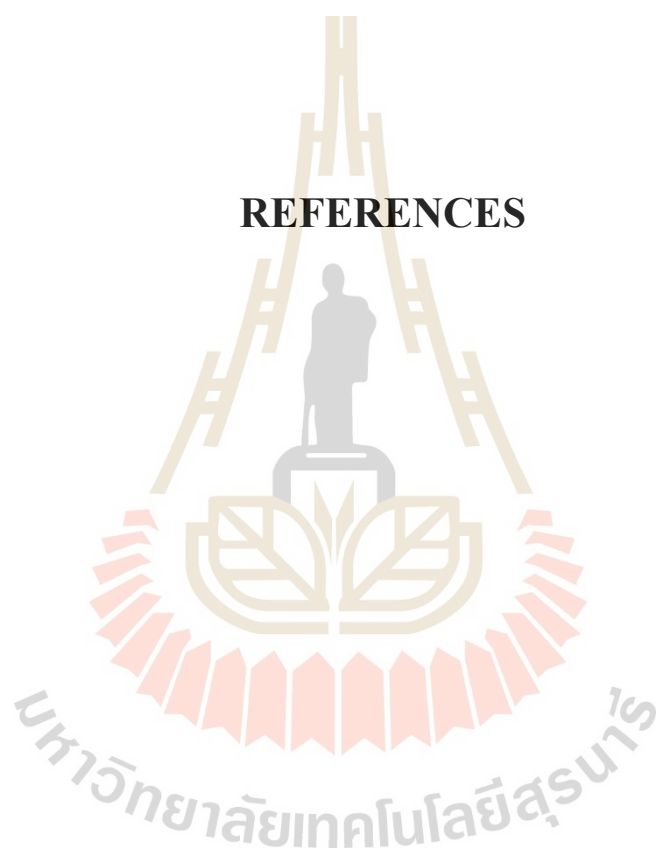
In this thesis, SnO₂ was grown on Si (001) substrate by MBE technique. The experiment was carried out by deposition of Sn layers and subsequent oxidation in air at room temperature. The growth mechanism was real-time observation by in-situ LEEM and LEED. The result shows that the Sn layer was formed but did not entirely cover the substrate surface. The surface morphology of the grown layer was studied by AFM. It was observed that the growth follows the Volmer-Werber island growth mode according to the C-AFM and ESM measurement. The formation of the three-dimensional structure of the grown SnO₂ layer with a size of approximately 100 nm was observed. The chemical composition of the grown SnO₂ layer was confirmed by XPS. However, it was found that the grown Sn layer was not completely oxidized after air exposure at room temperature. The growth mechanism and chemical composition results indicate that the grown SnO₂ appears as the quantum dots.

The effect of substrate temperature between 150-300°C on the growth was also studied. It was found that the SnO₂ grown at different substrate temperatures have the similar morphology, but they are different in the density of the island on the Si substrate. The SnO₂ grown at the substrate temperature of 225°C the smallest size and highest density of islands of 80 nm and 53%, respectively were observed on the SnO₂ grown at the substrate temperature of 225°C.

The optical properties of the grown SnO₂ quantum dot at the different substrate were also studied by PL. The emission of all the grown SnO₂ quantum dot show the emission peaks at 450(2.76 eV), 467 (2.66 eV), and 478 (2.60 eV) nm which are in the blue region (~440 -490 nm). This result suggests the formation of high level of oxygen vacancy in the structure.



REFERENCES



REFERENCES

- Bera, D., Qian, L., Tseng, T. K., and Holloway, P. H. (2010). Quantum dots and their multimodal applications: a review. **Materials**. 3(4): 2260-2345.
- Gleiter, H. (2000). Nanostructured materials: basic concepts and microstructure. **Acta materialia**. 48(1): 1-29.
- Chakraborty, S., and Menon, K. S. (2019). Growth and surface structural study of tin oxide films on Ag (001). **Vacuum**. 160: 371-377.
- Choi, W. K., Sung, H., Kim, K. H., Cho, J. S., Choi, S. C., Jung, H. J., and Jeong, K. (1997). Oxidation process from SnO to SnO₂. **Journal of materials science letters**. 16(19) : 1551-1554
- Ganose, A. M., and Scanlon, D. O. (2016). Band gap and work function tailoring of SnO₂ for improved transparent conducting ability in photovoltaics. **Journal of Materials Chemistry C**. 4(7): 1467-1475.
- Bahade, S. T., Lanje, A. S., and Sharma, S. J. (2017). Synthesis of SnO₂ Thin Film by Sol-gel Spin Coating technique for Optical and Ethanol Gas Sensing Application. **Int. J. Sci. Eng**. 3: 567.
- Bai, G., Wu, Z., Li, J., Bu, T., Li, W., Li, W., and Zhong, J. (2019). High performance perovskite sub-module with sputtered SnO₂ electron transport layer. **Solar Energy**. 183: 306-314.
- Bendjedidi, H., Attaf, A., Saidi, H., Aida, M. S., Semmari, S., Bouhdjar, A., and Benkhetta, Y. (2015). Properties of n-type SnO₂ semiconductor prepared by spray

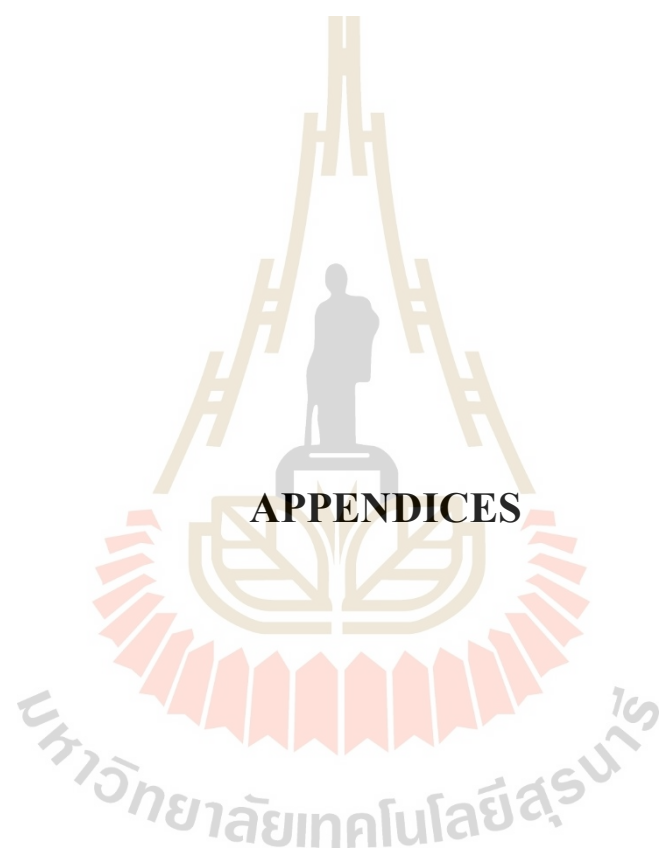
- ultrasonic technique for photovoltaic applications. **Journal of Semiconductors**. 36(12): 123002
- Bera, D., Qian, L., Tseng, T. K., and Holloway, P. H. (2010). Quantum dots and their multimodal applications: a review. **Materials**. 3(4): 2260-2345.
- Chakraborty, S., and Menon, K. S. (2019). Growth and surface structural study of tin oxide films on Ag (001). **Vacuum**. 160: 371-377.
- Chen, J. S., and Lou, X. W. (2013). SnO₂-based nanomaterials: synthesis and application in lithium-ion batteries. **small**. 9(11): 1877-1893.
- Choi, W. K., Sung, H., Kim, K. H., Cho, J. S., Choi, S. C., Jung, H. J., and Jeong, K. (1997). Oxidation process from SnO to SnO₂. **Journal of materials science letters**. 16(19): 1551-1554
- Das, S., and Jayaraman, V. (2014). SnO₂: A comprehensive review on structures and gas sensors. **Progress in Materials Science**. 66: 112-255.
- Fauzia, V., Yusnidar, M. N., Lallasari, L. H., Subhan, A., and Umar, A. A. (2017). High figure of merit transparent conducting Sb-doped SnO₂ thin films prepared via ultrasonic spray pyrolysis. **Journal of Alloys and Compounds**. 720: 79-85.
- Filevska, L. M. (2018). Luminescence of nanoscale tin dioxide. Review. **PACS** 73.61. (27): 52-59.
- Franchi, S. (2013). Molecular beam epitaxy: fundamentals, historical background and future prospects. **Elsevier**. In Molecular Beam Epitaxy pp.1-46.
- Ganose, A. M., and Scanlon, D. O. (2016). Band gap and work function tailoring of SnO₂ for improved transparent conducting ability in photovoltaics. **Journal of Materials Chemistry C**. 4(7): 1467-1475.

- Gleiter, H. (2000). Nanostructured materials: basic concepts and microstructure. **Acta materialia**. 48(1): 1-29.
- Hishita, S., Janeček, P., and Haneda, H. (2010). Epitaxial growth of tin oxide film on TiO₂ (1 1 0) using molecular beam epitaxy. **Journal of crystal growth**. 312(20): 3046-3049.
- Jain, P., Singh, S., Siddiqui, A. M., and Srivastava, A. K. (2017). Microstructural characteristics and optical performance of nano-structured thin films of tin oxide. **Indian Journal of Pure & Applied Physics (IJPAP)**. 55(6): 385-393.
- Javed, S., Islam, M., and Mujahid, M. (2019). Synthesis and characterization of TiO₂ quantum dots by sol gel reflux condensation method. **Ceramics International**. 45(2): 2676-2679.
- Kar, A., Kundu, S., and Patra, A. (2011). Surface defect-related luminescence properties of SnO₂ nanorods and nanoparticles. **The Journal of Physical Chemistry. C**, 115(1): 118-124.
- Khan, A. F., Mehmood, M., Aslam, M., and Ashraf, M. (2010). Characteristics of electron beam evaporated nanocrystalline SnO₂ thin films annealed in air. **Applied Surface Science**. 256(7): 2252-2258
- Kim, H. J., and Lee, J. H. (2014). Highly sensitive and selective gas sensors using p-type oxide semiconductors: Overview. **Sensors and Actuators B: Chemical**. 192: 607-627.
- Kim, H. Y., Nam, J. H., George, S. M., Park, J. S., Park, B. K., Kim, G. H., and Han, J. H. (2019). Phase-controlled SnO₂ and SnO growth by atomic layer deposition using

- Bis (N-ethoxy-2, 2-dimethyl propanamido) tin precursor. **Ceramics International**. 45(4): 5124-5132.
- Kim, H. Y., Nam, J. H., George, S. M., Park, J. S., Park, B. K., Kim, G. H., and Han, J. H. (2019). Phase-controlled SnO₂ and SnO growth by atomic layer deposition using Bis (N-ethoxy-2, 2-dimethyl propanamido) tin precursor. **Ceramics International**. 45(4): 5124-5132.
- Kumar, B., Atla, V., Brian, J. P., Kumari, S., Nguyen, T. Q., Sunkara, M., and Spurgeon, J. M. (2017). Reduced SnO₂ porous nanowires with a high density of grain boundaries as catalysts for efficient electrochemical CO₂ - into-HCOOH conversion. **Angewandte Chemie International Edition**. 56(13): 3645-3649.
- Kwoka, M., and Krzywiecki, M. (2017). Impact of air exposure and annealing on the chemical and electronic properties of the surface of SnO₂ nanolayers deposited by rheotaxial growth and vacuum oxidation. **Beilstein journal of nanotechnology**. 8(1): 514-521.
- Kwoka, M., Ottaviano, L., Passacantando, M., Santucci, S., Czempik, G., and Szuber, J. (2005). XPS study of the surface chemistry of L-CVD SnO₂ thin films after oxidation. **Thin Solid Films**. 490(1): 36-42.
- Liu, H., Zhang, W., Yu, H., Gao, L., Song, Z., Xu, S., and Tang, J. (2015). Solution-processed gas sensors employing SnO₂ quantum dot/MWCNT nanocomposites. **ACS applied materials & interfaces**. 8(1): 840-846.
- Mai, L., Zanders, D., Subaşı, E., Ciftiyurek, E., Hoppe, C., Rogalla, D., and Bock, C. (2019). Low-Temperature Plasma-Enhanced Atomic Layer Deposition of Tin (IV) Oxide from a Functionalized Alkyl Precursor: Fabrication and Evaluation of SnO₂-

- Based Thin-Film Transistor Devices. **ACS applied materials & interfaces**. 11(3): 3169-3180.
- Morresi L., (2013). Basics of molecular beam epitaxy (MBE) technique. **Silicon based thin solar cells**. 81-107.
- Nath, S. S., Ganguly, A., Gope, G., and Kanjilal, M. R. (2017). SnO₂ quantum dots for nano light emitting devices. 8(5).
- Nikiforov, A., Timofeev, V., Mashanov, V., Azarov, I., Loshkarev, I., Volodin, V., and Korolkov, I. (2020). Formation of SnO and SnO₂ phases during the annealing of SnO (x) films obtained by molecular beam epitaxy. **Applied Surface Science**. 512: 145735.
- Selvi, E. T., Sundar, S. M., Selvakumar, P., and Ponnusamy, P. M. (2017). Structural, optical and magnetic properties of SnO₂ quantum dot. **Journal of Materials Science: Materials in Electronics**, 28(11): 7713-7723.
- Sharma, S., Srivastava, A. K., and Chawla, S. (2012). Self assembled surface adjoined mesoscopic spheres of SnO₂ quantum dots and their optical properties. **Applied surface science**. 258(22): 8662-8666.
- Tan, M. (2018). Low-Cost Growth of Sustainable Fluorine-Doped SnO₂ Thin Films as a Transparent Conductive Electrode for Field Emission Lighting.
- Um, J., and Kim, S. E. (2014). Homo-junction pn diode using p-type SnO and n-type SnO₂ thin films. **ECS Solid State Letters**. 3(8): P94-P98.
- Venables, J. (2000). Introduction to surface and thin film processes. Cambridge University Press.

- W. Guo, L. Fu, Y. Zhang, K. Zhang, L. Y. Liang, Z. M. Liu, H. T. Cao, and X. Q. Pan (2010) Microstructure, optical, and electrical properties of p -type SnO thin films. **Appl. Phys. Lett.** 96: 042113.
- White, M. E., Tsai, M. Y., Wu, F., and Speck, J. S. (2008). Plasma-assisted molecular beam epitaxy and characterization of SnO₂ (101) on r-plane sapphire. **Journal of Vacuum Science & Technology A: Vacuum, Surfaces, and Films**, 26(5): 1300-1307.
- Yang, G., Chen, C., Yao, F., Chen, Z., Zhang, Q., Zheng, X., and Ke, W. (2018). Effective Carrier-Concentration Tuning of SnO₂ Quantum Dot Electron-Selective Layers for High-Performance Planar Perovskite Solar Cells. **Advanced Materials**. 30(14): 1706023.
- Yang, G., Chen, C., Yao, F., Chen, Z., Zhang, Q., Zheng, X., and Ke, W. (2018). Effective carrier-concentration tuning of SnO₂ quantum dot electron-selective layers for high-performance planar perovskite solar cells. **Advanced Materials**, 30(14): 1706023.
- Yu, Y., Zhu, Y., Guo, J., Yue, H., Zhang, H., Liu, C., and Liang, B. (2018). Suppression of TiO₂ photocatalytic activity by low-temperature pulsed CVD-grown SnO₂ protective layer. **Industrial & Engineering Chemistry Research**, 57(26): 8679-8688.
- Zhang, Q., Liu, Y., Blum, R. S., Han, J., and Tao, D. (2018). Sparse representation based multi-sensor image fusion for multi-focus and multi-modality images: A review. **Information Fusion**. 40: 57-75.



APPENDICES

APPENDIX A

SIZE AND AREA OF ISLAND MEASUREMENT

In this work, size and density of cluster or island were estimated by the ImageJ version 1.52a software.

1. Size estimation

1.1 Open the program by click this icon . When the program opens, the window is shown as in Figure A.1.

1.2 Firstly, select the file for analysis. Click the “File” and then click open command to import an image file. The program show the selected image and then click the “straight” to create the line in the image as shown in Figure A.2.

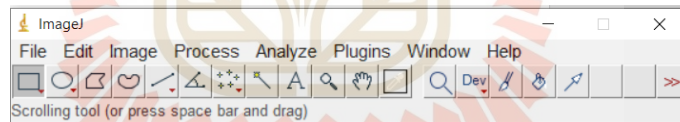


Figure A.1 Main window of ImageJ software.

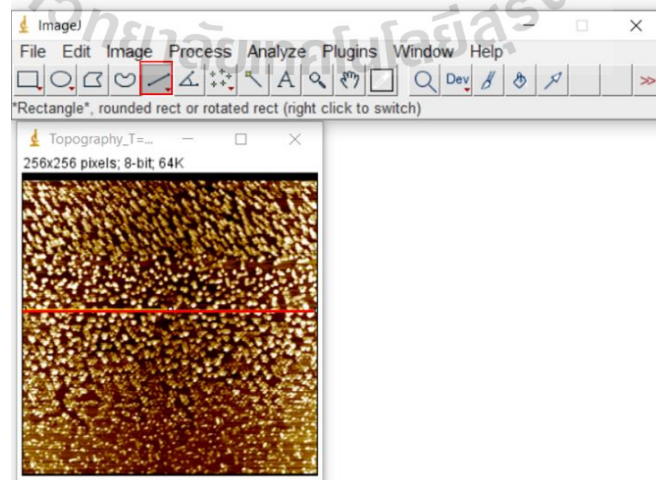


Figure A.2 Main window of ImageJ software after import an image file.

1.3 Click “Analyzer” tool and choose the “Set scale” command, Then the program shows a new window as shown in FigureA3 and FigureA.4.

1.4 Adjust “Known distance” to 5 and “Unit of length” to micrometer (um) and then click “OK” to set the scale.

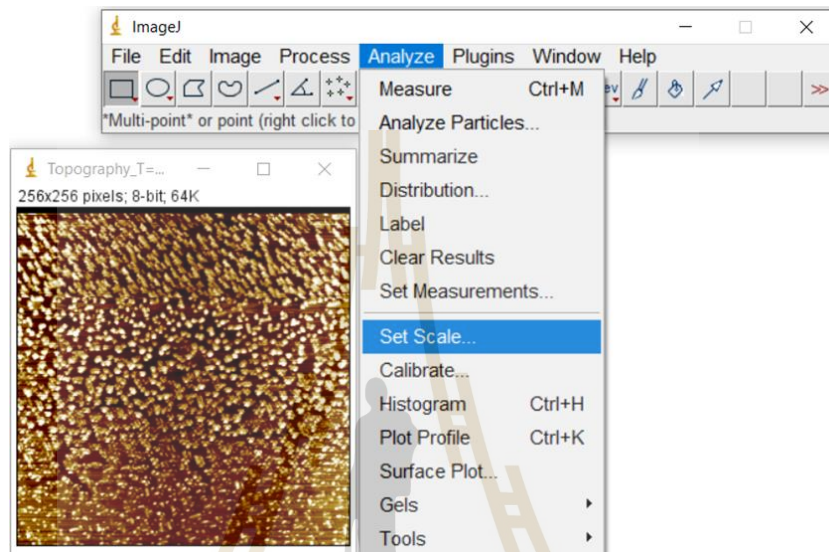


Figure A.3 Process of scale setting.

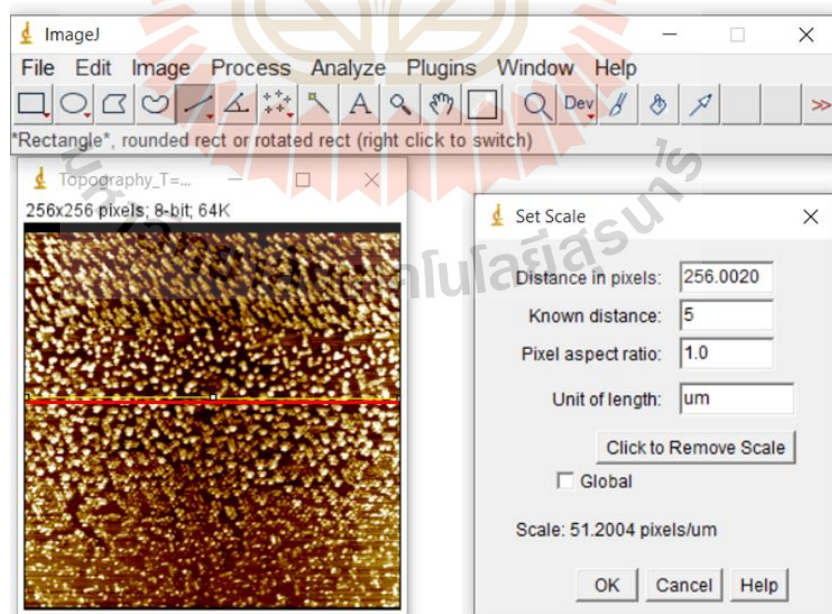


Figure A.4 New window for adjustment of known distance and unit of length.

1.5 Click “Straight” command again and then create the line in the dimension of an island (Red line), click “Analyze” tool and measure command.

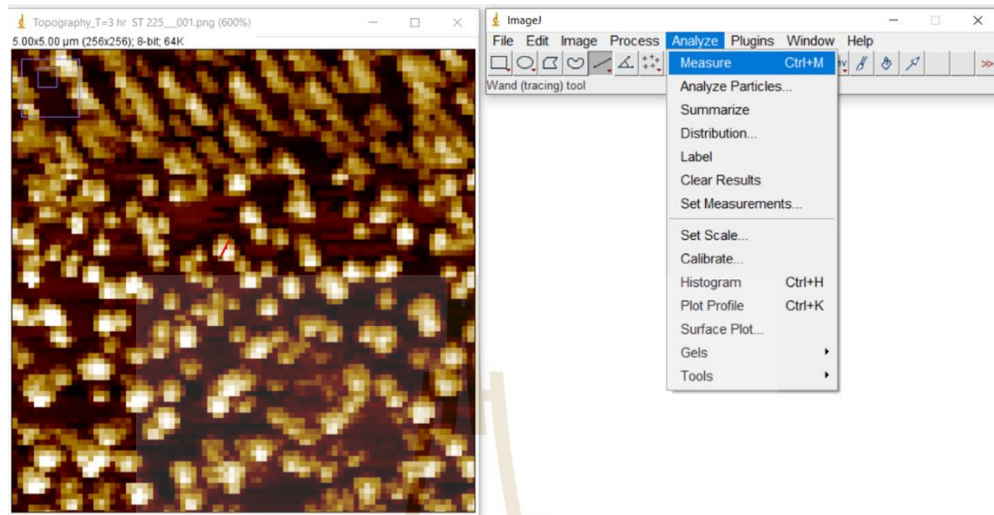


Figure A.5 Window shows the measurement command.

1.6 New pop-up window appear. The new window shows the parameter on the table. The dimension of island are shown in the “Length” column as shown in Figure A.6.

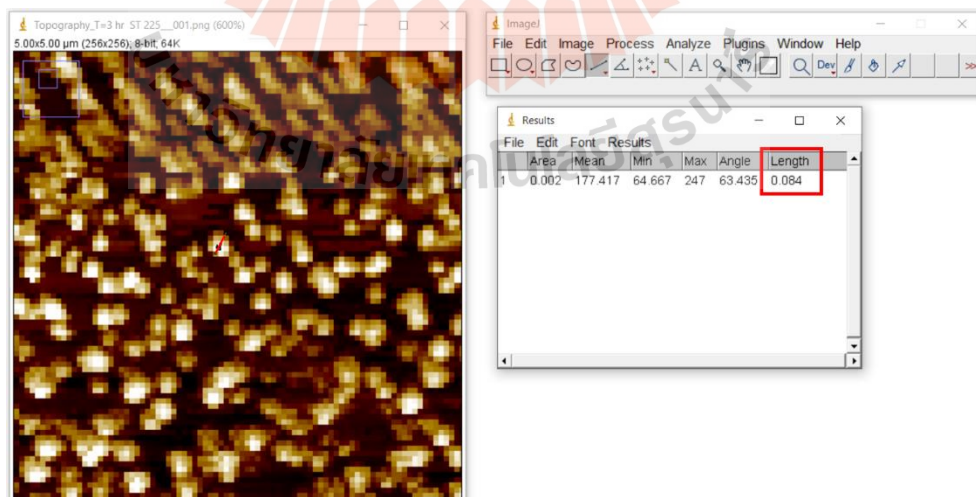


Figure A.6 Window after click measure command.

1.7 Measure the island from about 100-150 data point for one sample as shown in Figure A.7, and then the value of length is averaged.

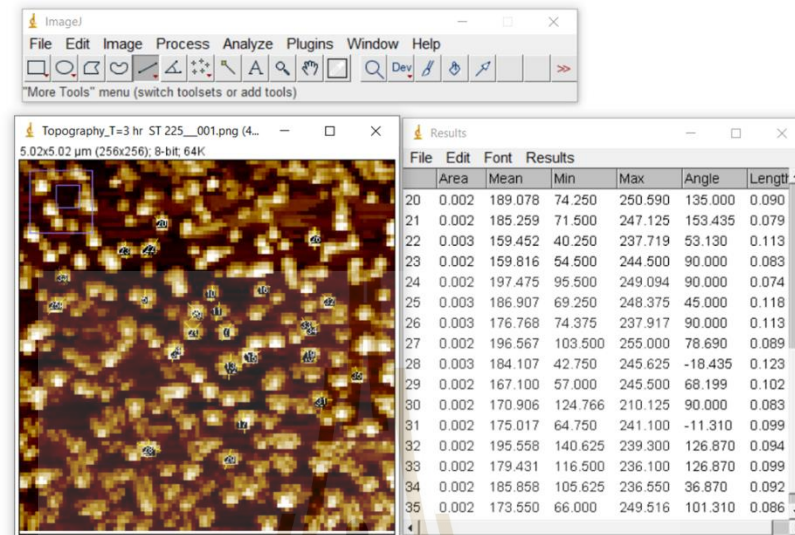


Figure A.7 Image after the estimation.

2. Area measurement

2.1 The first step of area measurement is as same as 1.1 to 1.5 of size measurement. Then, click “Image” tool and choose “Threshold” command (or Ctrl+shift+T) as shown in Figure A8. The program appears a new window.

2.2 Adjust the value for moving red cursor while change the value. The red area have to cover the island. Then, click “Apply”.

2.3 The image change to the black-white mode as shown in Figure A10. Next, click analyze tool and choose “Analyze particle”. The program shows a new window. Adjust the show parameter to “Bare outline” and then click OK.

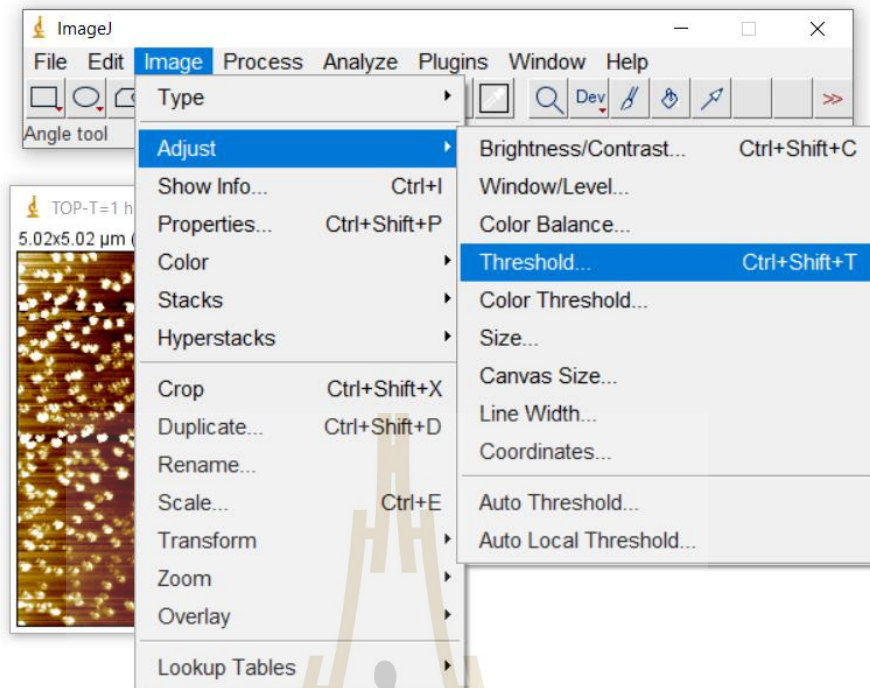


Figure A.8 “Threshold” command in the program.

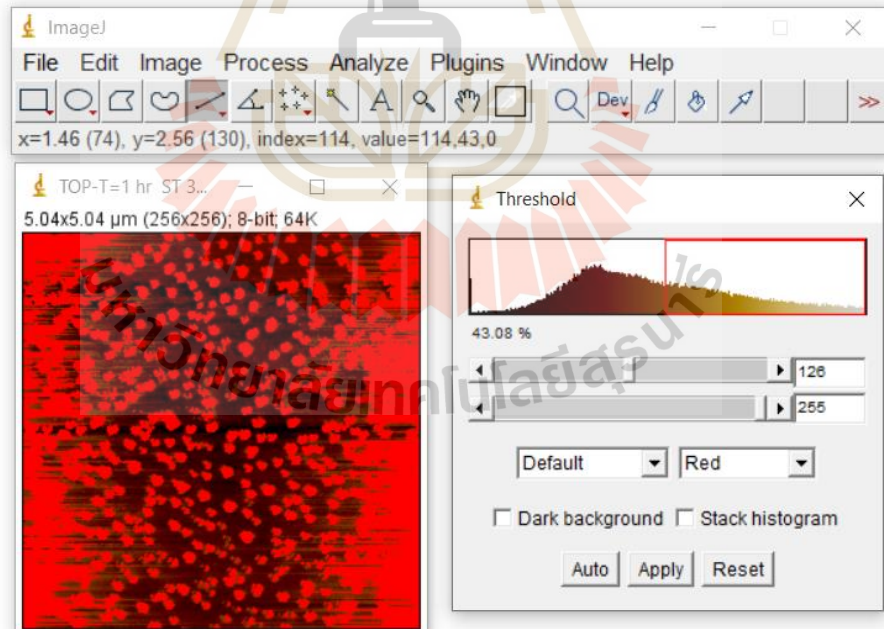


Figure A.9 Adjustment of the selected area for calculation.

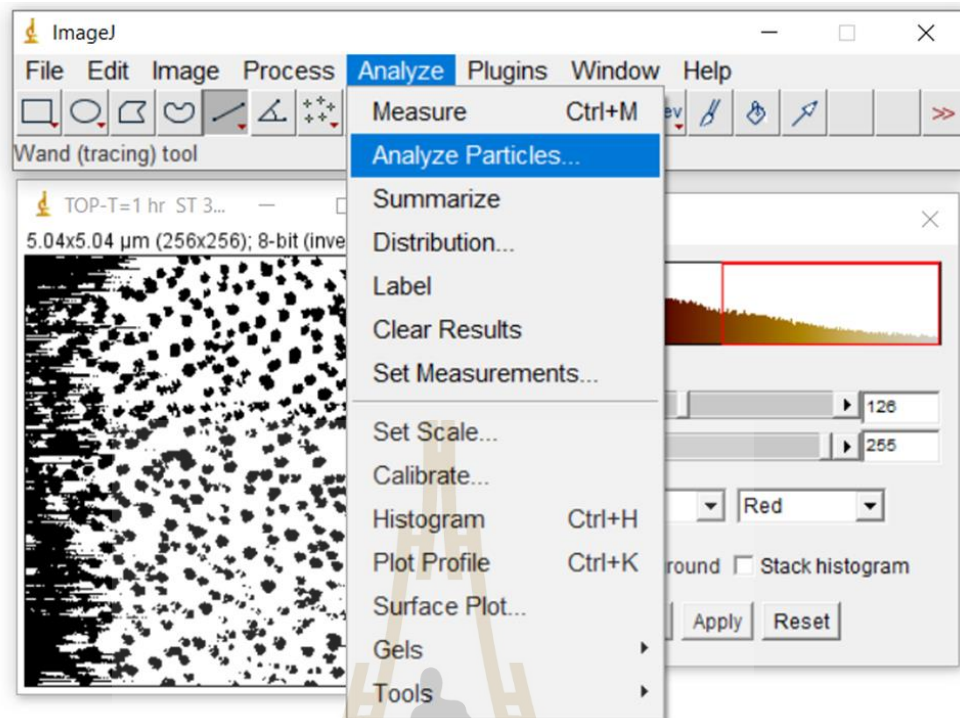


Figure A.10 “Analyze Particles” command.

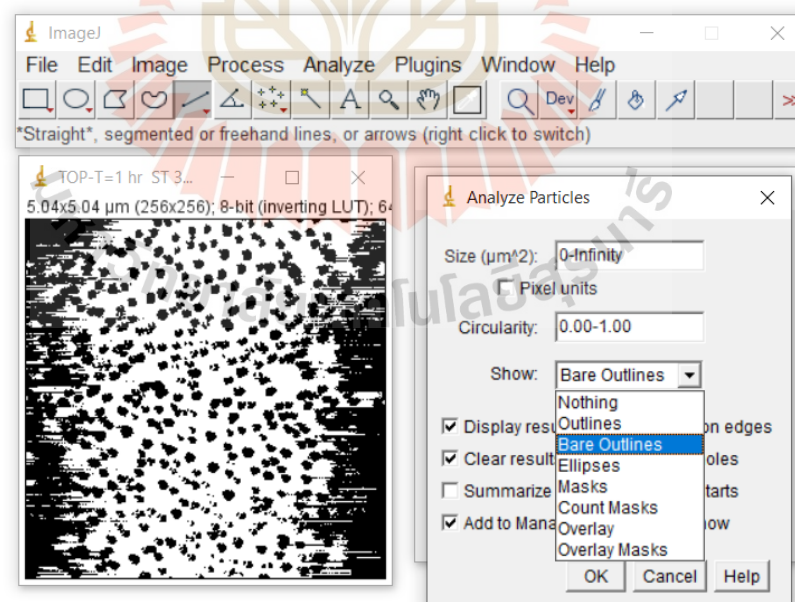


Figure A.11 “Bare Outlines” function in the shown parameter.

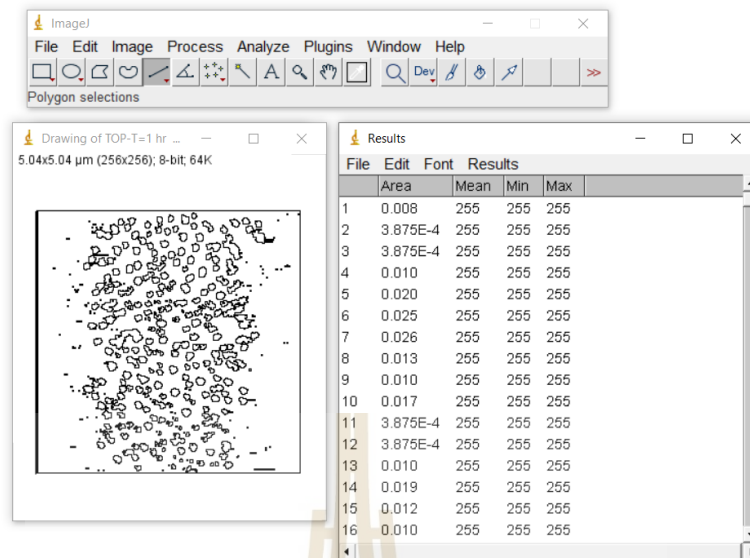
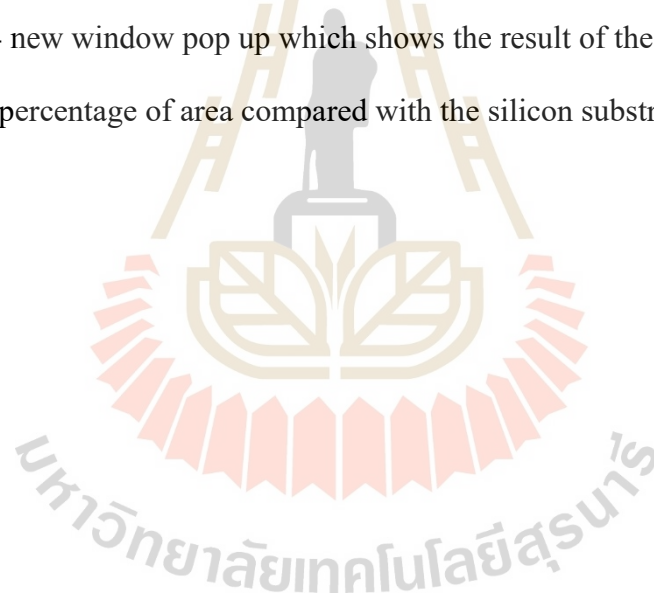


Figure A.12 Window shows the result of area.

2.4 new window pop up which shows the result of the island's area. Then, calculate the percentage of area compared with the silicon substrate's area.



APPENDIX B

COMPONENTS AND OPERATION OF E-FLUX ELECTRON BEAM EVAPORATOR

1. Components of e-flux electron beam evaporator

Evaporator consists of eight components which are shown in Figure B.1.

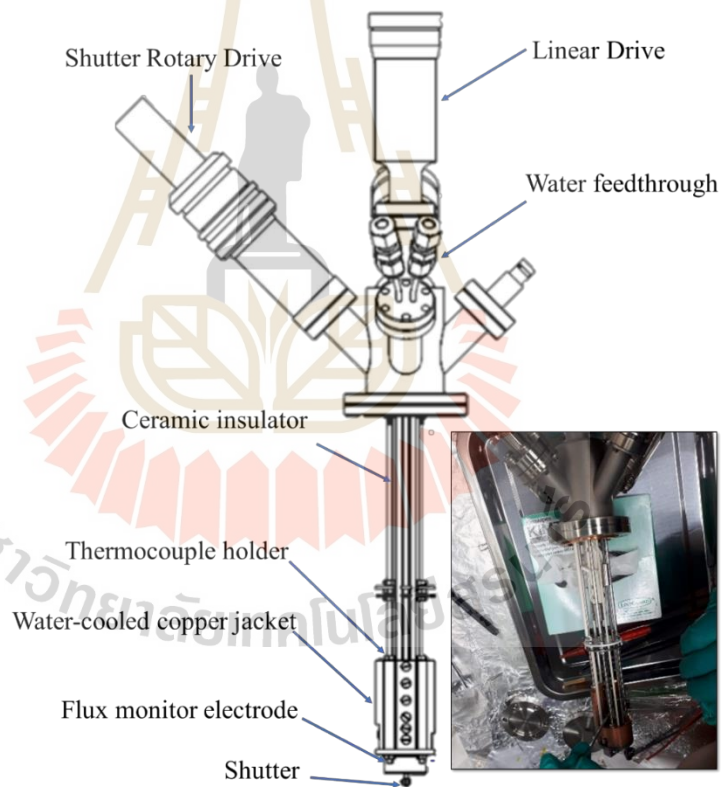


Figure B.1 General assembly drawing of evaporator.

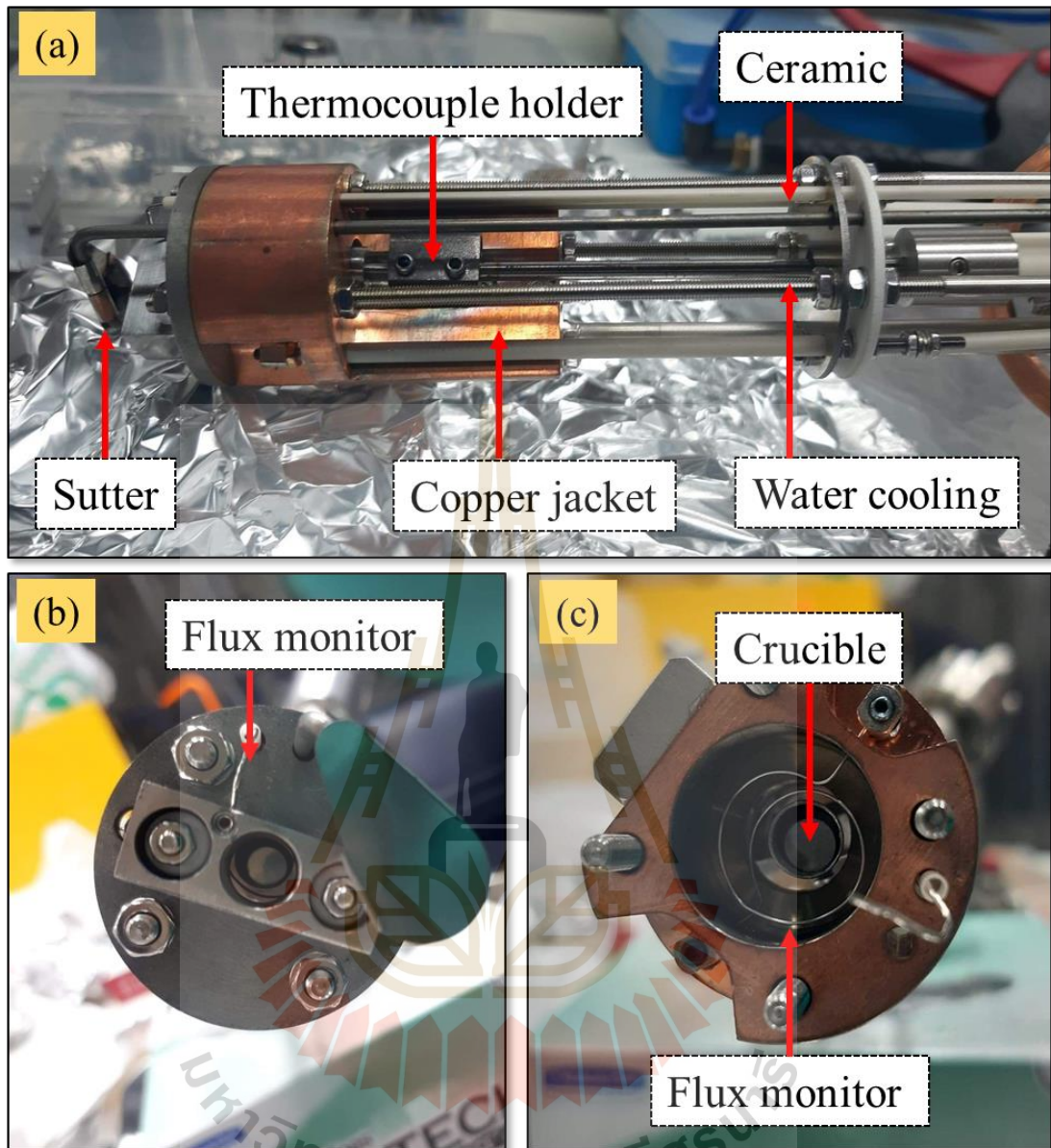


Figure B.2 Evaporator from tetra company, (a) beside of the evaporator, (b) top-view (c) inside copper jacket.

2. Operation of e-flux electron beam evaporator

The source should not be operated in a chamber pressure greater than 1×10^{-5} Torr. Operation at pressure higher than this can cause random and high current arc

discharges occurring around the HV part of the evaporator. Such discharges can lead to severe damage of equipment.

2.1 Heating source material (Sn powder)

- Open the power supply (Figure B.3) and increase the emission a little.
- Slowly increase the high voltage (control pressure) to 1 kV.
- Slowly increase the filament until the LED light goes out and then increase the filament a little.
- Slowly increase the emission until the LED light goes out.
- Observe the flux current and pressure in the experimental chamber during increase the filament and the emission.
- Control the flux current of atomic beam to about 50 nA the value of emission to about 12 mA and filament to about 6.5A as shown in Figure (B.3)(b).

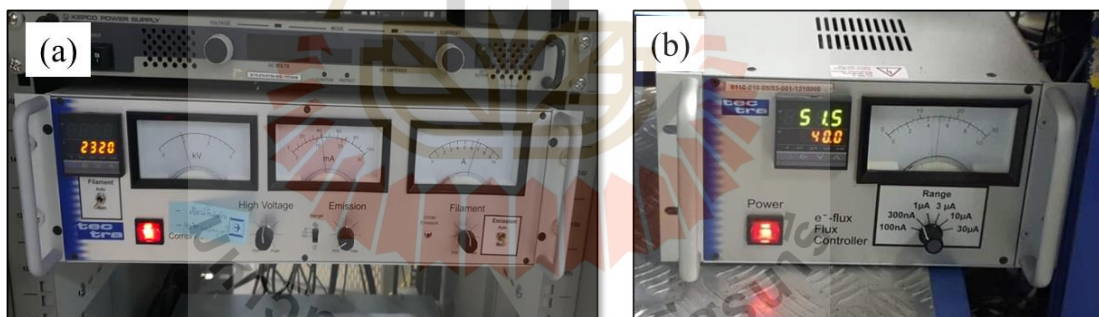


Figure B.3 (a) Power supply for controlling the flux current and (b) flux controller.

CURRICURUM VITAE

Name Dechmongkhon Kaewsuwan

Date of Birth 28 July 1993

Place of Birth Nakhonsawan, Thailand

Education

- 2011 – 2014 Bachelor of Science in Applied Physics, Department of Physics, Faculty of Science, Naresuan University, Phitsanulok, Thailand
- 2018 – present Master of Science in Applied Physics, School of Physics, Institute of Science, Suranaree University of Technology, Nakhon Ratchasima, Thailand

Publication

- Plerdsranoy, P., Kaewsuwan, D., Chanlek, N., & Utke, R. (2017). **Effects of specific surface area and pore volume of activated carbon nanofibers on nanoconfinement and dehydrogenation of LiBH₄**. International Journal of Hydrogen Energy, 42(9), 6189-6201.
- Sitthiwet, C., Thiangviriyaya, S., Thaweelap, N., Meethom, S., Kaewsuwan, D., Chanlek, N., & Utke, R. (2017). **Hydrogen sorption and permeability of compacted LiBH₄ nanoconfined into activated carbon nanofibers impregnated with TiO₂**. Journal of Physics and Chemistry of Solids, 110, 344-353.
- Plerdsranoy, P., Thiangviriyaya, S., Dansirima, P., Thongtan, P., Kaewsuwan, D., Chanlek, N., & Utke, R. (2019). **Synergistic effects of transition metal halides and activated carbon nanofibers on kinetics and reversibility of MgH₂**. Journal of Physics and Chemistry of Solids, 124, 81-88.